The Hong Kong Polytechnic University

Department of Electronic and Information Engineering

Reconstruction of Super-resolution Image from Low-resolution Images Using Adaptive Wiener Filtering

ZHANG Xiang

A thesis submitted in partial fulfillment of

the requirements for the degree of

Master of Philosophy

August 2010

CERTIFICATE OF ORIGINALITY

I hereby declare that this thesis is my own work and that, to the best to my knowledge and belief, it reproduces no material previously published or written, nor material that has been accepted for the award of any other degree or diploma, except where due acknowledgement has been made in the text.

_____(Signed)

ZHANG Xiang (Name of student)

To my parents

ABSTRACT

Super-resolution image reconstruction is an image fusion issue in which multiple low resolution images are fused into a higher resolution image. Among the various approaches proposed to realize super-resolution image reconstruction, the approach proposed by Hardie in 2007 is one of the efficient approaches as it is based on adaptive Wiener filtering (AWF) in which only weighted summation of the observed low resolution pixels is required in the core process of the estimation of the high resolution pixels.

In Hardie's AWF algorithm, the weights are derived with an isotropic covariance model based on (1) the geometric distance between two samples and (2) the local variance of the observed low resolution pixels in the region of interest. Though this simple model reflects the correlation of two pixels in the general situation to a certain extent, it is not appropriate to describe the pixel correlation in a local region with presence of edge or texture. Obviously, the covariance model adopted in AWF plays a significant role to the success of the algorithm. In this work, we devote our effort to improve the covariance model so as to improve the performance of AWF and investigate the impact of the covariance model to the performance of AWF.

Hardie's covariance model adapts to the local sample variance only and does not take the edge characteristics into account. In practice, pixels are more correlated in a non-edge region than an edge region as an edge breaks the correlation between the pixels in different sides of the edge. A simple trick is exploited in our first attempt to improve the model. In particular, separate covariance models are trained for edge regions and non-edge regions. To process an image, local regions are classified into either edge regions or non-edge regions, and then corresponding covariance models are used to derive the weights for individual regions.

The success of the simple trick exploited in our first attempt confirms the direction of improvement. The idea is further extended to improve the covariance

model. Obviously, pixels along an edge should be more correlated than those pixels in different sides of the edge. As a result, the covariance model function should be anisotropic according to the edge orientation in a local region. In our second attempt, we evaluate the sample variances along various directions in a local region and, based on the evaluation result, adjust the shape of covariance model function. By doing so, the orientation of the covariance model function and the extent of its asymmetricity are fully adaptive to the local characteristics. Unlike the approach adopted in our first attempt, no explicit region classification is required.

Though a visible improvement in the super-resolution image reconstruction performance can be achieved with the aforementioned improved covariance models, there is still room for further improvement. To a certain extent, our second attempt tries to detect the edges and then rectify the covariance model according to the detected edge direction. This is not always an easy task. For example, it is not easy to detect a complicated edge especially when it is in a texture or noisy region. Besides, since the high resolution image is not available, the detection has to be based on the available low resolution images and hence the detection may not be accurate. To solve this problem, in the third proposed solution we add an additional element to the covariance model to take care of the edge characteristics implicitly such that no explicit edge detection is required.

In general, the more two pixel's intensity values are different, the more likely that the two pixels are separated by an edge or corrupted by noise. Based on this observation, a new covariance model is defined to be a function of both the intensity difference and the geometric distance of two pixels. Without any explicit edge detection, the model automatically deemphasizes the correlation between two pixels which are not in the same side of an edge. Accordingly, the weights of the pixels for estimating the high resolution pixels can be determined more reliably with the covariance model, and a better super-resolution image reconstruction result can be obtained at the end.

AUTHOR'S PUBLICATIONS

International Journal Papers

1. Kyle Xiang Zhang, Yuk-Hee and Wan-Chi Siu,, "A Patch based Wiener Filter for Super Resolution Reconstruction," *submitted for possible publication in Journal of Electronic Imaging.*

International Conference Papers

1. Kyle Xiang Zhang, Yuk-Hee and Wan-Chi Siu, "An iterative super-resolution algorithm based on adaptive wiener filtering," to be appeared in Proceeding of APSIPA Annual Summit and Conference 2010, Singapore, Dec 14-17 2010.

2. Kyle Xiang Zhang, Yuk-Hee and Wan-Chi Siu,, "Realizing super resolution with directional anisotropic correlation model," Proceeding of the 7th IEEE International Conference on Information, Communication and Signal processing (ICICS'09), pp.656-659, Macau, China, Dec 8-10, 2009.

3. Kyle Xiang Zhang, Yuk-Hee and Wan-Chi Siu, "An improved wiener filter for super resolution," Proceeding of APSIPA Annual Summit and Conference 2009, pp.821-824, Sapporo Japan, Oct 4-7, 2009.

ACKNOWLEDGEMENTS

I would like to take this opportunity to express my sincere gratitude to The Hong Kong Polytechnic University, where I started my research work. My major appreciation should be given to both my chief supervisor Dr. Chris Y. H. Chan and my co-supervisor Prof. W. C. Siu, for their patient guidance, professional advice, continuous support and encouragement, concerning to my research and especially the attitude of life. It is a great honor for me to work with them. I have significantly benefited from the numerous discussions with them on every stage of the study. Without their help, understanding and patience, it is impossible for me to achieve current level and complete this research study.

Furthermore, I would like to give sincere appreciation to my colleagues, Dr. K. H. Chung and Dr. Y. H. Fung, who are supervised by my chief supervisor as well. During the period of research study, they shared their best research experience, skills and understanding with me, which greatly helps me. Also, I would like to thank all people working in the center for multimedia signal processing, such as Dr. Kenneth K. M. Lam, Dr. Y. L. Chan, Dr. Bonnie N. F. Law, Dr. K. O. Cheng, Dr. Calvin H. K. Cheung, Mr. W. H. Wong, Mr. C. Xu and Mr. W. L. Hui and so on so forth.

I would also like to express my best wishes and appreciation to all other academic staff and administrative staff of the department. They have established a good and nice academic and living environment for me to work here.

Last but not least, I must express my heartfelt gratitude to my parents, my friends and Miss. X. W. Xu for their understanding, endless support and encouragement. Without them, there is no chance for me to finish this research study.

TABLE OF CONTENTS

LIST OF ABBREVIATIONS

AWF	Adaptive Wiener Filtering
CCD	Charge-Coupled Device
HDTV	High Definition TV
HPF	High Pass Filter
HR	High Resolution
HVS	Human Visual System
IBP	Iterative Back Projection
LCC	Local Context Classifier
LR	Low Resolution
LPF	Low Pass Filter
LMSE	Least Mean Square Error
ML	Maximum Likelihood
MAP	Maximum a posteriori
MSE	Mean Square Error
NSR	Noise-to-Signal Ratio
POCS	Projection onto Convex Set
PSNR	Peak Signal-to-Noise Ratio
PSF	Point Spread Function
SR	Super Resolution
SSE	Sum of Square Error

LIST OF FIGURES

LIST OF TABLES

STATEMENT OF ORIGINALITY

The following contributions reported in this thesis are claimed to be original.

1. An adaptive Wiener filtering algorithm which classifies local regions and then applies corresponding covariance models to derive the filter weights for individual regions.
2. An adaptive Wiener filtering algorithm which exploits a directional intensity covariance model to make the filter weights adaptive to the dominant edge orientation in a region.
3. An adaptive Wiener filtering algorithm which rectifies the spatial intensity covariance of each pair of pixels in a local region with their observed or estimated low resolution samples such that the Wiener filter in the region can fully adapt to the local context of the region without explicit edge detection.

Chapter 1

INTRODUCTION

1.1 Super Resolution Problem

Images of high resolution are normally desired and even required in many electronic imaging applications such as remote sensing, medical imaging and remote monitoring. They are desired as they can offer more details that may be critical to the applications. For example, in remote sensing applications, high resolution aerial images can help scientists to gather more detail information from the earth ground such that an accurate analysis on the ground activities can be made.

Nowadays CCD and CMOS image sensors are widely used to capture digital images. The recent advance in sensor technology has already made a digital camera capable of supporting a resolution of 4096×2304. However, as compared with the resolution supported by an analog 35 mm film, it is still far from the ideal. Hence, there is always a need to increase the current resolution level.

The most direct solution to increase spatial resolution is to increase the number of pixels in a unit area of the sensor array of a camera by sensor manufacturing techniques. This can be achieved by reducing the size of the sensors in the sensor array. However, the amount of light that a sensor can sense also decreases and it is easier for the sensors to suffer from noise. As a matter of fact, there is a limitation of

sensor size reduction and the current image sensor technology has almost reached this level.

Another possible approach to increase spatial resolution is to increase the number of sensors in a sensor array. This increases the chip size and, in turns, the capacitance of the sensors. Accordingly, the response time of the sensor array slows down and the camera performance is degraded. This solution does not end up with a high performance camera.

After all, the success of the aforementioned solutions rely on the advance of optical and sensor technologies. The high cost for high precision optics and image sensors may not be affordable in many commercial applications. A low-cost solution is required to increase the spatial resolution under the limitations of current sensors and optics manufacturing technology.

Under this consideration, perhaps a more practical solution is to use multiple images of lower resolution to reconstruct a high resolution image by making use of some signal processing techniques. This approach is called super-resolution image reconstruction or simply super-resolution, and has become an active research area. The major advantage of this signal processing approach is that it costs less and the existing imaging systems can still be utilized.

In many practical cases, it is possible for one to obtain multiple images of the same scene under a controlled manner. For example, in satellite imaging applications, several images of the same area can be captured from different positions in the orbit. The relative positions that the satellite captures the images can be precisely controlled by the time it takes the photos. The displacement of the satellite, and its camera, introduces a relative global motion of the captured area in successive images. One can shift the captured images according to their relative motion vectors and mount them to a predefined two-dimensional reference space. This process is referred to as registration. As long as there are some sub-pixel relative scene motions from image to image, the number of samples in the reference space is more than the number of

samples in a single low resolution image, and hence extra information is available for one to construct the high resolution image. This explains why super-resolution is feasible to increase the spatial resolution with the existing imaging systems at a low cost.

The previous example shows the case when the low resolution images are obtained by the same camera at different instants. It is also possible that the low resolution images are obtained by different cameras positioned under a controlled manner at the same time. It is also possible that the images are captured by different cameras at different instants. Figure 1.1 shows the various scenarios that a super-resolution is done.

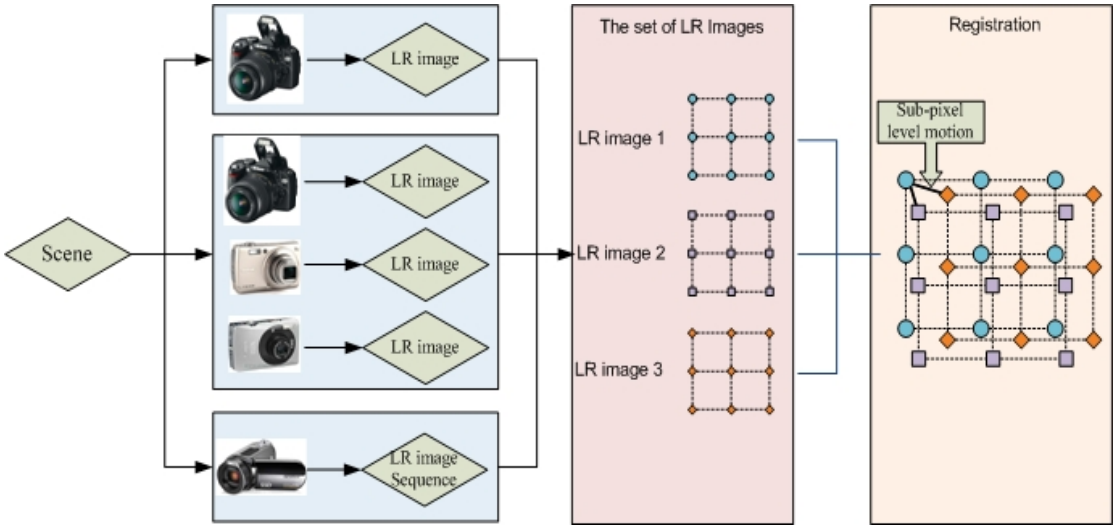

Figure 1.1 Basic premise for super-resolution image reconstruction

After registration, we have a number of samples mounted to a reference two-dimensional space. In general, their positions do not align with a uniform grid of the desirable resolution and their total number is still smaller than the required number of samples needed to fill up the desirable resolution grid. Besides, in the process of recording a digital image, there are natural distortions caused by the optical distortion, motion blur and sensor noise as shown in Figure 1.2. In other words, every available sample in the reference space is actually a corrupted sample of a low resolution version of the desirable high resolution image. From that point of view, the

reconstruction of the high resolution image from the collection of low resolution image samples can be treated as an image restoration problem.

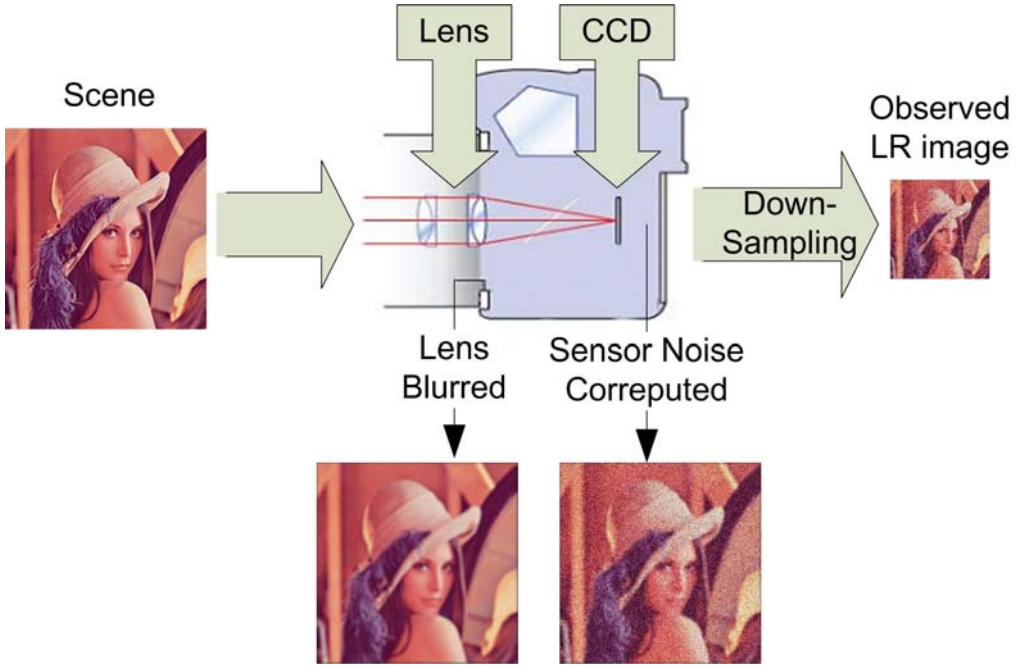

Figure 1.2 Illustration of a simple physical image formation process. Ideal signal is blurred by lens and then corrupted with sensor noise before down-sampling.

Various image restoration techniques can be applied to realize super-resolution image reconstruction, which results in a number of super-resolution algorithms. These algorithms can be roughly categorized into four groups. The first category tackles the problem in the frequency domain based on the connection between the frequency spectra of a high resolution image and its low resolution images. The second category tries to establish a correspondence between a high resolution image and its low resolution versions based on some training data through a machine learning technique, and then use the machine to realize super-resolution in the future. The third category models the conversion process that turns a high resolution image into a low resolution image, makes an initial estimate of the high resolution image, and then repeatedly refines its estimate until the refined estimate equals to the observed low resolution image after undergoing the modeled conversion process. The final category is based on interpolation. Registered low resolution samples in a local region are weighted and summed to estimate a high resolution sample in the same region. Consequently, the estimation is locally adaptive to the image content. This category of algorithms is simple yet effective in providing a good super-resolution result, and hence arouses our interest to carry out a study on it.

The adaptive Wiener filtering algorithm proposed by Hardie[Hardie07] is a typical example of this interesting category of algorithms. In this algorithm, the weights of the low resolution samples in a local region are adjusted according to (i) the local characteristic of the region and (ii) the spatial distance of the low resolution samples from the estimated high resolution sample. To achieve this, the algorithm models the intensity covariance between two high resolution pixels in a local region as a function of (i) the variance of the observed low resolution samples registered in the region and (ii) the geometric distance between the two high resolution pixels, and then derives the weights based on this covariance model. Hardie's adaptive filtering approach [Hardie07] has been proven to be an effective approach to realize super-resolution. In the work presented in this thesis, it is used as a vehicle to study the potential of interpolation-based algorithms.

Obviously, the spatial intensity covariance model adopted in Hardie's adaptive Wiener filtering algorithm [Hardie07] plays a significant role to the success of the algorithm. Though this model is helpful to derive a locally adaptive Wiener filter for estimating the high resolution samples, there is still room for improvement as it does not take the edge characteristics into account. In this work, we devote our effort to improve the covariance model so as to improve the performance of adaptive Wiener filtering in super-resolution image reconstruction.

Three major improvements were made in our study and they are reported in this thesis. They are proposed based on the following three beliefs. First, pixels are more correlated in a non-edge region than an edge region in practice as an edge breaks the correlation between the pixels in different sides of an edge. The covariance model for regions having an edge should be different from the covariance model for regions without an edge.

Second, pixels along an edge are more correlated then pixels in different sides of the edge. As a result, the covariance model should not be formulated as an isotropic function as the one proposed in Hardie's approach. Instead, it should be anisotropic according to the edge orientation in a local region.

Any pairs of pixels in the same region follow the same covariance model in Hardie's algorithm when deriving the weights of the Wiener filter for the region. In fact, each pair of pixels should have its own covariance model as intensity correlation is different from pair to pair.

Three corresponding modifications to the covariance model used in Hardie's algorithm are suggested in this work. These modifications result in three adaptive Wiener filtering algorithms for super-resolution image reconstruction.

1.2 Organization of thesis

This thesis comprises six chapters in total. Apart from this chapter, the reminder of this thesis is organized as follows.

Chapter 2 presents a brief review on the background knowledge related to super-resolution image reconstruction. In particular, a common observation model of images that formulates the connection among a scene, its low resolution images and its high resolution image is introduced. Various conventional approaches for tackling super-resolution image reconstruction are briefly discussed. Our focus is on the interpolation-based approach. As a typical example of the kind, the adaptive Wiener filtering algorithm [Hardie07] recently proposed by Hardie is comprehensively elaborated in this chapter. This algorithm is used as the vehicle in our study presented in this work.

Chapter 3 presents our first modification to improve the performance of adaptive Wiener filtering in super-resolution image reconstruction. Local regions are classified as either edge regions or smooth regions such that the spatial intensity covariance model used for deriving the Wiener filter coefficients can be adaptive to the local characteristics of a local region. This results in a new adaptive Wiener filtering algorithm for super-resolution image reconstruction. Its performance is evaluated and reported in this chapter.

To extend the idea exploited in the development of the algorithm proposed in Chapter 3, one can further adjust the spatial intensity covariance model based on the dominant orientation of the edges in a local region. Based on this idea, Chapter 4 presents a new directional anisotropic covariance model. This model formulates the intensity correlation among pixels in a local region according to the regional context. It results in another new adaptive Wiener filtering algorithm to do super-resolution image reconstruction. Simulation results are reported to show the improvement of this algorithm as compared with the original adaptive Wiener filtering algorithm [Hardie07] in terms of various performance criteria.

In Chapter 5, a further improved adaptive Wiener filtering algorithm is proposed. In this algorithm, each pair of pixels in a local region has its spatial intensity covariance model rectified by their known observed low resolution samples. In other words, every single pair of pixels has its own covariance model. As a result, a covariance model and accordingly a local Wiener filter are possible to fully adapt to the local context. Unlike the algorithm proposed in Chapter 4, no explicit edge detection is required. Simulation results show that this proposed adaptive Wiener filtering algorithm is able to provide the best performance among the suggested improvements to the original adaptive Wiener filtering algorithm [Hardie07].

The thesis is concluded in Chapter 6 with a summary of the work that has been done in this project. Possible future work and potential extension of the present work are discussed in this chapter as well.

Chapter 2

BACKGROUND OF SUPER-RESOLUTION IMAGE RECONSTRUCTION

2.1 Introduction

This chapter provides reviews on some existing work that is relevant to our work. In particular, a popular observation model shared by many super-resolution image reconstruction algorithms is first presented in Section 2.2. This observation model is critical to super-resolution image reconstruction as it describes the relationship between the target high resolution image and the available distorted low-resolution versions of the image. In Section 2.3, conventional super-resolution image reconstruction methods are categorized and some of their examples are briefly introduced. Among these various methods, the one based on adaptive Wiener filtering[Hardie07] arouses our interest due to its simplicity and effectiveness in providing a good super-resolution image reconstruction performance. In the final section of this chapter, this adaptive Wiener filtering algorithm is discussed in depth as it is used as a vehicle for us to carry out the study reported in this thesis.

2.2 Observation Model

Super-resolution image reconstruction aims to enhance the spatial resolution of

an image with the fusion of multiple low resolution images. Super-resolution image reconstruction algorithms are built based on an observation model which models the physical imaging process. This observation model plays a critical role in the development of a super-resolution image reconstruction algorithm.

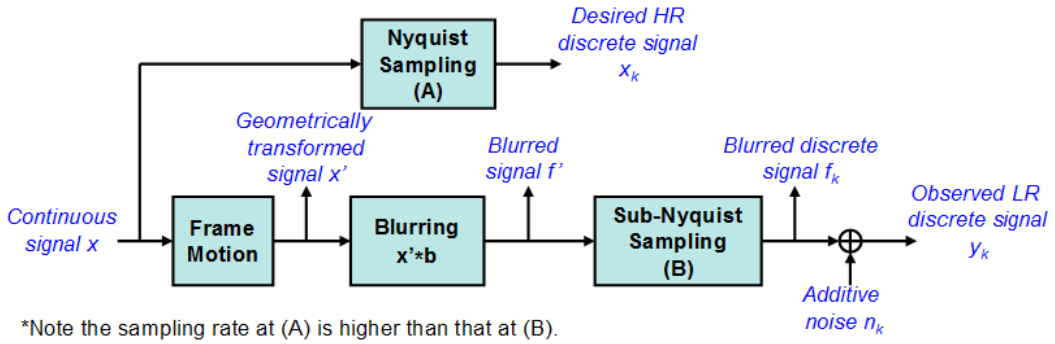

(a)

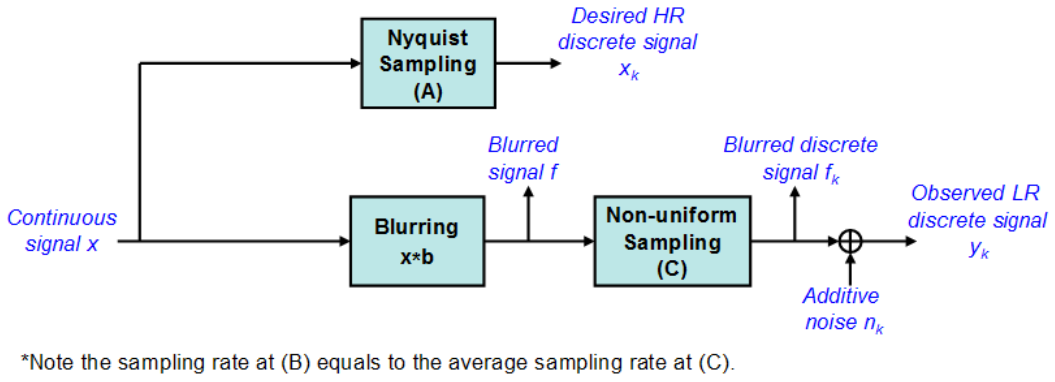

(b)

Figure 2.1 (a) The classic model of how an observed LR frame is generated from a continuous 2D signal, and (b) an alternative model of (a) when the blurring function is linear spatially invariant and circularly symmetric

Figure 2.1 (a) shows an observation model that is commonly adopted in many super-resolution image reconstruction algorithms nowadays. This model is derived from the real physical process of image formation. To produce a high resolution (HR) image, the original continuous signal x should be sampled at or above Nyquist frequency to get the desired discrete samples of x.

Due to some practical constraints, multiple low resolution (LR) images of X are obtained instead. Theoretically, multiple LR images provide more information of

signal X than a single LR image such that one can construct the HR image based on the LR images. There could be a relative motion of the camera with respect to X between two capturing processes, so any LR image is considered to be an image of a geometrically transformed version of signal *x*. Note that here we assume that *x* is time-invariant. If it is not, the process could be too complicated to be formulated with a simple observation model. Even so, the involved motion can result in a combined rotation and translation or even an affine transformation of *x*. In this work, we put our focus on aerial image and video applications in which the involved motion is basically translation.

The image capturing process of a camera converts the geometrically transformed continuous signal *x* into a LR image. Due to the optical distortions caused by the camera, the motion blur introduced by the slow shutter speed, sensor noise, and insufficient sensor density, the geometrically transformed *x*, *x*', is blurred and corrupted with noise before being sampled below the Nyquist frequency. In formulation, we have

$$y = \mathrm{D}(b * \mathrm{G}(x)) + n \tag{2.1}$$

where $*$ is the convolution operator, **D** is an sampling operator, **G** is a geometrical transformation operator, *b* is a blurring function and *n* is a random noise. In general, *b* is assumed to be a Gaussian low pass filter. Thus, *y* is a discrete signal after sampling from continuous signal *x*.

When the blurring function is linear spatially invariant and circularly symmetric, the observation model can be simplified as the one shown in Fig.1(b). All the work reported in this thesis is based on this observation model.

2.3 Conventional Approaches

Various conventional super-resolution image reconstruction algorithms have

been proposed. They can be approximately classified into four categories including transform-domain algorithms [Bose93, Huang84, Kim90, Kim93], machine learning-based algorithms [Freeman02, Jiji06], iterative reconstruction algorithms [Baboulaz09, Costa08, Chiang00, Dai09, Elad97, Farsiu04, Farsiu06, Fransens07, Fan06, He07, Hardie98, He09, Irani91, Keren88, Li10, Nguyen01, Protter09A, Protter09B, Segall04, Shen07, Tuinstra99, Takeda09, Takeda07, Tian10, Zomet01, Zhang10] and interpolation-based algorithms [Goldberg03, Hardie07, Naray07, Nguyen00, Pham06, Sanchez08]. They are briefly introduced in this section. For more details, one can refer to individual papers and the tutorial papers about conventional super-resolution image reconstruction algorithms [Borman98, Kang03, Ng06].

2.3.1 Transform-domain approaches

The super-resolution image reconstruction problem is initially addressed in the frequency-domain by Tsai and Huang [Huang84]. This frequency domain approach is based on three major principles: i) the shifting property of Fourier transform, ii) the relationship between the continuous Fourier transform of the original signal and the discrete Fourier transform of the observed signal, and iii) the assumption that the original signal is band-limited.

Let $x(m,n)$ be the original continuous signal and $X(u,v)$ be its continuous Fourier transform result. Suppose we have N shifted versions of $x(m,n)$ and the k^{th} shifted image is expressed as $x_k(m,n) = x(m+\Delta m, n+\Delta n)$. According to the shifting property of Fourier transform, the Fourier transform of x_k is

$$X_k(u,v) = X(u,v)e^{j2\pi(\Delta m \cdot u + \Delta n \cdot v)} \tag{2.2}$$

The k^{th} observed LR image $y_k(m,n)$ is obtained by sampling $x_k(m,n)$ with

horizontal and vertical sampling period T_1 and T_2. By making use of the aliasing relationship and a bandlimitedness assumption, one can formulate $Y_k(u,v)$, the discrete Fourier transform of $y_k(m,n)$, as a function of $X(u,v)$.

The relationship between $Y_k(u,v)$ and $X(u,v)$ can be reformulated as a matrix equation in a form as $Y = \Psi X$, where Y is a column vector containing the transformed coefficients of all N observed signal, X is a column vector containing the transformed coefficients of the unknown original signal, and Ψ is a matrix which is the operator that maps X to Y. By finding Ψ, $x(m,n)$ can be recovered through the inverse transformation of X.

Bose et. al. [Bose93] proposed to use recursive total least square to minimize the registration error. Kim et.al [Kim90, Kim93] further extended the work in [Huang84] with a recursive least square approach for motion blurred and noisy conditions. Although the frequency-domain approach is computationally inexpensive and intuitively simple, it is sensitive to modeling error [Kang03] and hence its use is limited.

2.3.2 Machine learning-based approaches

Machine learning-based approaches [Freeman02, Jiji06] are technically based on the establishment of a correspondence between LR image and HR image through different machine learning techniques. The learning process is to estimate the joint probability of random variables, where all missing pixel values are considered as random variables. Calculating joint probability $P(x,y)$ directly is a NP-hard problem and hence approximation is required.

Maximum Likelihood (ML) and Maximum a posteriori (MAP) are two conventional estimators for predicting a random variable x. Both of them are based on Bayes' theorem, $P(x \mid y) = P(y \mid x) \cdot P(x) / P(y)$. Random variable x is estimated as

$x = \arg\max\{P(y \mid x)\}$ and $x = \arg\max\{P(x \mid y) \cdot P(y)\}$ respectively when ML and MAP are used. It is normally to take the corresponding logarithmic function and optimize it with respect to unknown variable *x*.

Prior knowledge is critical for estimating *x*. Freeman et al. [Freeman02] proposed to use Markov Random Field to model the relationship between a patch of LR samples and a patch of HR samples as prior. Jiji et. al. [Jiji06] proposed to use an off-line training based algorithm. It concentrates on edge patterns by learning edge patterns from extensive training. This sort of methods generally produces stable and good results in dedicated applications such as super-resolution for face recognition. However, as the performance heavily relies on the training result and a huge amount of effort is required in the training stage, it is comparatively not as flexible as other conventional methods. The focus of this thesis is mainly on the non-iterative optimization methods. Machine-learning approaches are hence out of the scope of this thesis.

2.3.3 Iterative reconstruction methods

Iterative reconstruction methods [Baboulaz09, Costa08, Chiang00, Dai09, Elad97, Farsiu04, Farsiu06, Fransens07, Fan06, He07, Hardie98, He09, Irani91, Keren88, Li10, Nguyen01, Protter09A, Protter09B, Segall04, Shen07, Tuinstra99, Takeda09, Takeda07, Tian10, Zomet01, Zhang10] iteratively refine an initial estimated HR image until the refinement converges. Three popular approaches are briefly discussed here as examples.

Deterministic Regularization

Deterministic regularization [Costa08, Farsiu04, Farsiu06, He07, Hardie98, Li10, Protter09A, Protter0B, Segall04, Takeda09, Takeda07, Vand07] is one of the major techniques used to solve super-resolution image reconstruction problem. The estimation of HR pixels from a set of LR samples is an inverse problem and it can be

solved with regularization by using some deterministic prior information about the possible solution. The prior information can possibly make inverse problem well-posed. For example, a possible solution can be obtained by minimizing the following objective function

$$\mathrm{J} = \left\| y - \Psi x \right\|^2 + \alpha \left\| Cx \right\|^2 \tag{2.3}$$

where the first term is the mean square error (MSE) related to the estimation and the second term is known as prior which provides a smooth constraint to the optimization process so as to find the solution. α is a Lagrange multiplier which makes a balance between the fidelity (MSE) and the smoothness (prior) criteria. If the objective function J is convex and differentiable, a unique solution of x can be found by minimizing function J with respect to x. Otherwise, there can be a lot of solutions which can only achieve local minima. The minimization of cost function J can be realized with iterative algorithms such as the gradient descent method in which the solution is iteratively estimated with

$$x_{k+1} = x_k - \beta \left. \frac{\partial J}{\partial x} \right|_{x=x_k} \tag{2.4}$$

where $$\left. \frac{\partial J}{\partial x} \right|_{x=x_k} = 2(\Psi^T \Psi + \alpha C^T C) \cdot x_k - 2\Psi^T y \tag{2.5}$$

is the gradient at $x=x_k$, β is a positive convergence parameter that controls the convergence and k is the iteration number.

Iterative Back Projection (IBP)

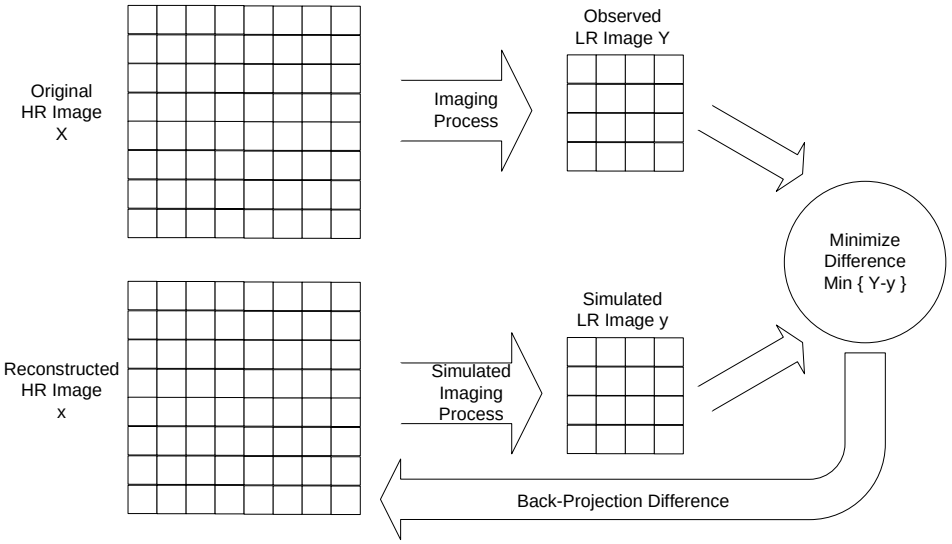

Fig 2.2 Illustration of Iterative Back Projection (IBP) program flow

IBP [Irani91, Keren88] is another class of methods to solve super-resolution image reconstruction problem. An observed LR image is formed as the result of a real imaging process. The iterative back projection technique simulates the imaging formation process to form a LR image from an initial estimated HR image and, based on the difference between the observed LR image and the simulated LR image, refine the estimated HR image.

Suppose that there are some LR images and the imaging processing operator for producing the k^{th} LR image from a HR image x^t is $\mathbf{I}_k$ as

$$y_k^t = \mathbf{I}_k(x^t) + n \tag{2.6}$$

where n is an additive noise. If x^t is the real original image and operator $\mathbf{I}_k$ is valid, y_k^t should be identical to the k^{th} observed image Y_k. Otherwise, there is an error between y_k^t and Y_k.

The target of IBP is to iteratively minimize

$$e = \sum_k \| Y_k - y_k^t \|^2 \tag{2.7}$$

by back projecting the error plane through a reversion process to x^t to generate x^{t+1}. Since there are more than one LR images and each one of them can make a contribution to the refinement, the error contributed by different LR pixels of different LR images are weighted as follows.

$$x^{t+1}(i,j) = x^t(i,j) + \sum_k \sum_{(m,n)\in\Psi_{k(i,j)}} (Y_k(m,n) - y_k^t(m,n)) \cdot \frac{h_{k(m,n)}}{c} \qquad (2.8)$$

where $\Psi_{k(i,j)}$ is a set of coordinates defining the locations of the LR samples in Y_k that is influenced by $x(i,j)$, $h_{k(m,n)}$ is a coefficient of the back projection kernel, and c is a normalization factor. The closer y_k^t gets to Y_k, the more x^t tends to be x.

The key to recover a better HR image is to define a proper back projection kernel, which significantly affects error back projection and indirectly influences the reconstruction performance.

Projection Onto Convex Set (POCS)

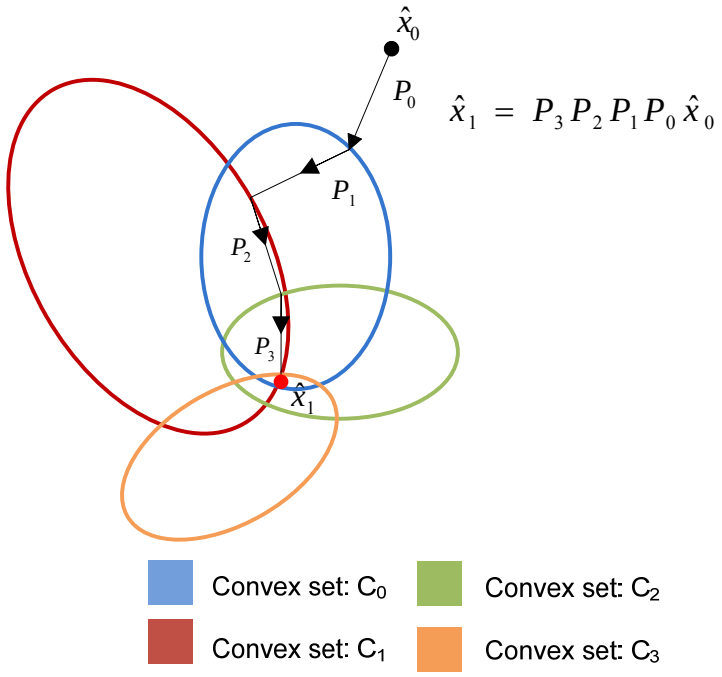

Figure 2.3 Illustration of POCS

POCS [Fan06] is an alternating iterative approach to find a solution satisfying a set of pre-defined constraints which are defined based on some prior information. This set of priors constrain the process to find the solution. In fact, if we have *N* priors and each of them is interpreted as a non-empty and closed convex set C_i, the solution will belong to the intersection set

$$C_s = \bigcap_{i=1}^{N} C_i \tag{2.9}$$

The intersection set C_s is a convex set as well.

To get the solution, an initial solution x_0 should be estimated and successive estimates are iteratively projected onto each of convex sets (prior) as follows.

$$x^{t+1} = \prod_{i=1}^{N} P_i \cdot x^t \tag{2.10}$$

where x^t is the estimate obtained at the t^{th} iteration and P_i is the projection operator which projects an intermediate estimate of the solution to convex set C_i.

The major advantages of POCS are that it is simple and it is possible to incorporate various types of prior information. However, POCS does not provide a unique solution and the convergence is generally slow.

2.3.4 Interpolation-based approaches

Interpolation-based approaches[Goldberg03, Hardie07, Naray07, Nguyen00, Pham06, Sanchez08] are intuitively simple and computationally efficient to estimate missing HR pixels. Relative displacement vectors of the available LR images with respect to the target HR image are first estimated by using sub-pixel motion

estimation techniques such that the LR images can be registered onto the HR grid for later interpolation. These displacement vectors are generally floating point vectors and hence a non-uniform interpolation is required to predict the pixels on the HR grid based on the registered LR pixels. A restoration process is generally followed to de-blur and denoise the interpolation result.

Narayanan et. al. [Naray07] proposed a computationally efficient super-resolution image reconstruction algorithm based on partition-based filter (PWS). For each local image region, this algorithm selects a filter from a set of pre-defined filters to do the interpolation. The filters are trained with some training images with vector quantization such that they can adapt to the local characteristic of a given region. Since the number of the filters in the set is finite, the adaptation capability of the filters is limited and there exists quantization error.

To solve this problem, Hardie [Hardie07] proposed a super-resolution image reconstruction algorithm by using adaptive Wiener filtering. An adaptive Wiener filter is used to estimate the missing HR pixels with the available LR pixels in the same local region. The filter adaptively adjusts its filter coefficients according to the local variance of the registered LR pixels, the local noise variance and the spatial correlation of the pixels in a local region. This provides a higher degree of flexibility in the adaptation and hence it is able to remove the noise effectively and produce a better reconstruction performance.

Interpolation-based approaches are generally noted for their simplicity and their relatively good super-resolution image reconstruction performance. This arouses our interest in exploring if it is possible to further improve their performance. As Hardie's adaptive filtering approach [Hardie07] has been proven to be a simple yet effective approach to realize super-resolution image reconstruction, it will be used as a vehicle for us to carry out our exploration study. In the following section, a brief summary of Hardie's adaptive Wiener filtering algorithm is provided as a basis for us to elaborate our work reported in this thesis.

2.4 Adaptive Wiener Filtering

Adaptive Wiener filtering is one of the efficient techniques for realizing super-resolution image reconstruction as only weighted summation of the observed low resolution pixels is required in the core process of the estimation of the high resolution pixels. The conventional adaptive Wiener filtering algorithm was proposed in [Hardie07] by Hardie. It derives the weights with a covariance model based on the geometric distance between two samples.

Super-resolution image reconstruction aims to enhance the spatial resolution of an image with the fusion of multiple LR images. As shown in Figure. 2.1(a), observed LR pixels in each LR image are generally considered as noisy samples of a blurred and geometrically transformed version of the original HR image. When the blurring function is linear spatially invariant and circularly symmetric, the observation model can be simplified as the one shown in Figure.2.1(b). Hardie's adaptive Wiener filtering algorithm [Hardie07] estimates the HR samples based on this model.

To start the process, all LR pixels in successive LR images are registered onto a plane on which there is a higher resolution grid defining the positions of the HR pixels to be estimated. Note that this high resolution grid also defines the coordinate system we used in this paper. Through a spatial sliding window covering a $3d \times 3d$ region of the high resolution grid, where d is the ratio of the target resolution of the reconstructed HR image to the resolution of a LR image for each dimension, Hardie's algorithm collects all LR pixels registered in the window to estimate the $d \times d$ HR pixels in the center of the window. Without losing the generality, we assume that the number of registered LR pixels in the window is L and the total number of HR pixels to be estimated with these L LR pixels is N. As an example, Figure. 2.4 shows the case when a HR image is constructed with 2 LR images and the ratio of their spatial resolutions is 3 for each dimension. In such a case, we have d=3, L=18 and N=9. For reference purpose, Ω_l and Ω_h are, respectively, used to denote the set of the locations of the observed LR pixels and the set of the locations of the HR pixels to be

estimated. In Figure 2.4, positions in Ω_l and Ω_h are, respectively, marked with crosses and circles.

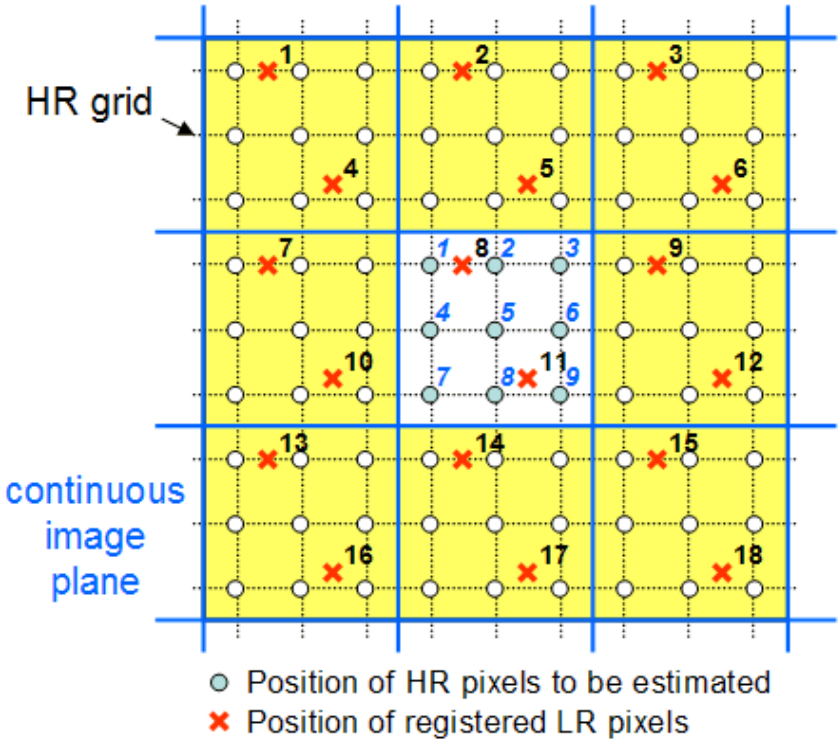

Figure.2.4 An example showing how LR pixels are involved in the estimation of the HR pixels in a patch

In Hardie's algorithm, the N HR pixels, denoted as $\vec{x} = [x_1, x_2, \ldots x_N]^T$ in vector form, are estimated as

$$\hat{x}_m = \frac{\sum_{k=1}^{L} \omega_{mk} y_k}{\sum_{k=1}^{L} \omega_{mk}} \quad \text{for } m=1,2\ldots N \tag{2.11}$$

where $\vec{y} = [y_1, y_2, \ldots y_L]^T$ are the registered LR pixels, $\hat{x}_m$ is the estimate of the m^{th} HR pixel and $\omega_{mk} / \sum_{n=1}^{L} \omega_{mk}$ is the normalized weight of the k^{th} LR pixel when estimating $\hat{x}_m$. Weights ω_{mk} is a particular coefficient of matrix W which is defined as

$$W = \begin{bmatrix} \omega_{11} & \omega_{21} & \cdots & \omega_{N1} \\ \omega_{12} & \omega_{22} & & \omega_{N2} \\ \vdots & & \ddots & \vdots \\ \omega_{1L} & \omega_{2L} & \cdots & \omega_{NL} \end{bmatrix} = R^{-1} \cdot P \tag{2.12}$$

where R is the auto-covariance matrix of $\{ y_k | k=1,\ldots L\}$ and P is the cross-covariance matrix of $\{ y_k | k=1,\ldots L\}$ and $\{ x_m | m=1,...N\}$.

By considering that the observed LR pixel y_k is corrupted with an additive zero mean random noise n and its noise-free version is $f_k = y_k - n_k$, where n_k is the noise value sampled at the position of LR pixel y_k, we have

$$R = E\{\vec{y} \cdot \vec{y}^T\} = E\{\vec{f} \cdot \vec{f}^T\} + \sigma_n^2 \cdot \mathrm{I} \tag{2.13}$$

and

$$P = E\{\vec{y} \cdot \vec{x}^T\} = E\{\vec{f} \cdot \vec{x}^T\} \tag{2.14}$$

where $\vec{f} = [f_1, f_2, \ldots f_L]^T$, $E\{\bullet\}$ is the expectation operator and σ_n^2 is the local variance of the noise.

In theory, f_k are samples of $\{f(i,j)\}$, a blurred version of the original HR image $\{x(i,j)\}$. In formulation, we have $f(i,j) = x(i,j) * b(i,j)$, where b is the blurring function. Accordingly, the cross-covariance of $x(i,j)$ and $f(i,j)$ and the auto-covariance of $f(i,j)$ can be, respectively, determined by

$$r_{fx}(i,j) = r_{xx}(i,j) * b(i,j) \tag{2.15}$$

and

$$r_{ff}(i,j) = r_{xx}(i,j) * b(i,j) * b(-i,-j) \tag{2.16}$$

In Hardie's algorithm, it is assumed that the covariance between two x samples can be modeled as

$$r_{xx}(\Delta i, \Delta j) = \sigma_x^{\,2} \cdot \rho^{\sqrt{\Delta i^2 + \Delta j^2}} \tag{2.17}$$

where $(\Delta i,\Delta j)$ is the distance of the two x samples, ρ (=0.75) is a tuning parameter that controls the decay of the auto-covariance with spatial distance and σ_x^2 is the local variance of x. In particular, σ_x^2 is estimated as

$$\sigma_x^2 = \max\left\{(\sigma_y^2 - \sigma_n^2)/C, 0\right\} \tag{2.18}$$

where σ_y^2 is the local variance of $\{y_k | k=1,\ldots L\}$ and

$$C = \int_{i=-\infty}^{\infty} \int_{j=-\infty}^{\infty} \rho^{\sqrt{i^2 + j^2}} \cdot (b(i,j) * b(-i,-j)) \cdot di \cdot dj \tag{2.19}$$

Elements of $E\{\vec{f} \cdot \vec{f}^{\,T}\}$ and $E\{\vec{f} \cdot \vec{x}^{\,T}\}$ in eqns. (2.13) and (2.14) and hence W can then be determined with $r_{ff}(\Delta i, \Delta j)$ and $r_{fx}(\Delta i, \Delta j)$, where $(\Delta i,\Delta j)$ is the distance of the two involved pixels.

Figure 2.5 shows the overall workflow of the algorithm. As mentioned earlier, this algorithm is simple yet effective in providing a good super-resolution image reconstruction performance, and hence is used in our study as a vehicle to explore the potential of interpolation-based super-resolution image reconstruction algorithms. To a certain extent, this algorithm is just a raw application of adaptive Wiener filtering and leaves much room for further improvement. In fact, the approach exploited in this algorithm forms a solution framework to handle super-resolution image reconstruction. Our contributions reported in this work are all developed based on this framework. In the following chapters, they will be discussed one by one.

For reference purpose, the algorithm presented in this section is considered as the conventional adaptive Wiener filtering algorithm for super-resolution image reconstruction and is referred to as AWFc hereafter in this thesis. Unless specifically specified, the interpretation of all variable notations appeared in Chapters 3, 4 and 5 follows the convention used in this section. All assumptions and conditions used in AWFc also apply to the algorithms presented in these chapters unless specifically specified.

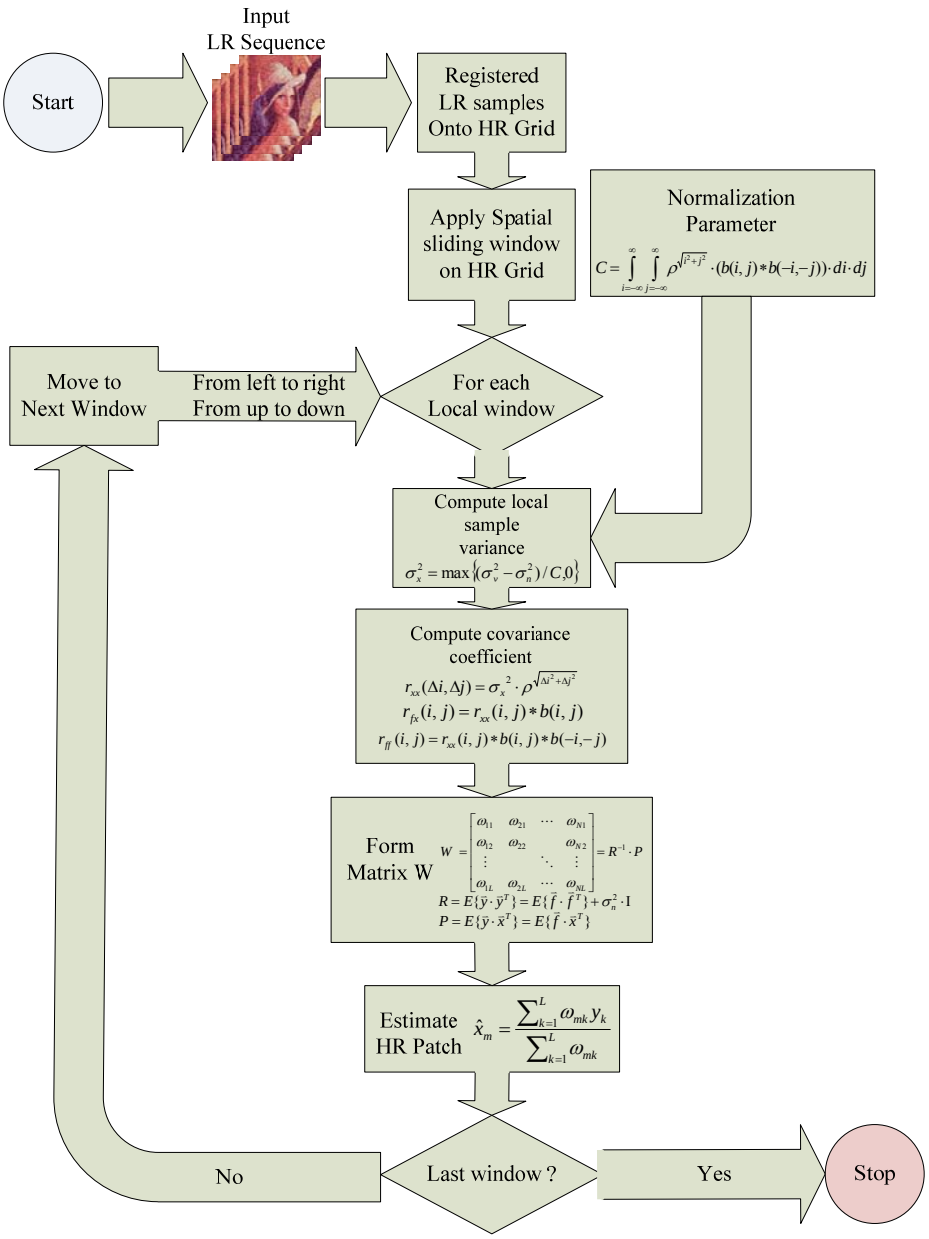

Figure 2.5 Overall workflow of conventional adaptive Wiener filtering [Hardie07] for super-resolution image reconstruction

Chapter 3

ADAPTIVE WIENER FILTERING WITH CLASSIFIED INTENSITY COVARIANCE MODELS

3.1 Introduction

In AWFc[Hardie07], a HR pixel is estimated to be a weighted sum of the registered LR pixels in its local region. From Section 2.4, one can see that the weight for each involved registered LR pixel is a function of (i) its distance from the HR pixel to be estimated and (ii) the local sample variance in the local region. The model of $r_{xx}(\Delta i, \Delta j)$ specified in eqn. (2.7) plays a significant role to determine the value of the weight.

AWFc's covariance model $r_{xx}(\Delta i, \Delta j)$ adapts to the local sample variance only and does not take the edge characteristics into account. Obviously, pixels are more correlated in a non-edge region than an edge region. An edge breaks the correlation between the pixels in different sides of the edge. AWFc may be able to handle a region containing a sharp edge to a certain extent as a sharp edge produces large local variance. However, for regions containing edges which introduce small intensity difference, its local variance may not be large enough to make AWFc's covariance

model reflect the real covariance among the pixels.

By considering the aforementioned factor, we suggest using two individual intensity covariance models for edge and smooth regions separately when deriving the weights of the registered LR pixels. Every local region in an image is classified as either an edge or non-edge region. A corresponding intensity covariance model is then used to derive the weights of the LR pixels in the region.

This chapter is organized as follows. In section 3.2, we show that, as compared with the original covariance model function used in AWFc[Hardie07], an exponential function can provide a better performance in modeling the local intensity covariance of an image. In Section 3.3, a classification scheme is proposed to classify local regions of a HR image to be estimated into edge regions or non-edge regions. When adaptive Wiener filtering technique is used, this allows one to exploit a more proper local covariance model to derive the weights of the available LR pixels for estimating the HR pixels in a local region. Two dedicated local intensity covariance models for regions of different nature are also derived in this section. In Section 3.4, simulation results are provided for comparing the performance of the proposed algorithm with the other state-of-the-art super-resolution image reconstruction algorithm. Finally, a brief summary is given in Section 3.5.

3.2 Exponential Covariance Function

In AWFc[Hardie07], the intensity covariance between two HR pixels are modeled as

$$r_{xx}(\Delta i, \Delta j) = \sigma_x^2 \rho^{\sqrt{\Delta i^2 + \Delta j^2}} \tag{3.1}$$

where (Δi,Δj) is the distance vector between two HR pixels, ρ is a tuning parameter that controls the decay of the autocorrelation with distance and σ_x^2 is the local variance of the HR image. This model is based on the assumption that the intensity

values of the samples along a particular direction can be modeled as a 1st order stationary Markov sequence with correlation coefficient ρ. In practice, due to the existence of edges and local textures, the assumption may not always be valid. In this section, we will show that the correlation between two pixels in an image is better to be modeled with an exponential function.

The idea of using an exponential function instead of eqn.(3.1) to model the intensity covariance between two HR pixels comes from the fact that an exponential function is more general. The classical central limit theorem states that the properly normed sum of a set of independent and identically distributed (i.i.d.) random variables will tend towards a normal distribution as the number of variables increases if each of these random variables is of finite variance. Without the finite variance assumption it becomes a stable distribution.

The characteristic function of a uni-variate stable distribution is given as [Levy87].

$$\varphi(t) = \exp(\, jbt - \gamma|t|^{\alpha}[1 + j\beta\, sign(t)\, \omega(t,\alpha)]) \tag{3.2}$$

where $b \in (-\infty,\infty),\ \gamma>0,\ \alpha \in (0,2],\ \beta \in [-1,1],$

$$\omega(t,\alpha) = \begin{cases} \tan(\frac{\alpha\pi}{2}), \text{ if } \alpha \neq 1 \\ \frac{2}{\pi}\log|t|, \text{ if } \alpha = 1 \end{cases}$$

and

$$sign(t) = \begin{cases} 1, & \text{if t} > 0 \\ 0, & \text{if t} = 0 \\ -1, & \text{if v} < 0 \end{cases}.$$

Parameter α is called characteristic exponent which controls the heaviness of the tail of the stable distribution. As shown in Figure 3.1, the smaller the value of α, the

heavier the tail is. Parameter γ determines the dispersion of the stable distribution. Parameters β and b are, respectively, the symmetric parameter and the shift parameter. For a symmetric stable distribution without shift, we have β=b=0. Accordingly, its characteristic function becomes an exponential function given as

$$\varphi(t) = \exp(-\gamma|t|^{\alpha}) \quad \text{where} \quad \gamma>0 \quad \text{and} \quad \alpha\in(0,2] \tag{3.3}$$

The intensity correlation of the pixels in a local region of a HR image can be modeled with a symmetric stable distribution function as $\varphi(\sqrt{\Delta i^2+\Delta j^2})$ = $\exp(-\gamma(\Delta i^2+\Delta j^2)^{\alpha/2})$, where $\sqrt{\Delta i^2+\Delta j^2}$ is the distance between two HR pixels. In such a case, the intensity covariance of the pixels in the region can be modeled as

$$r_{xx}(\Delta i,\Delta j) = \sigma_x^2 \exp\left(-\gamma(\Delta i^2+\Delta j^2)^{\alpha/2}\right) \quad \text{for} \quad \alpha\in(0,2],\ \gamma>0 \tag{3.4}$$

where σ_x^2 is the local intensity variance of the region.

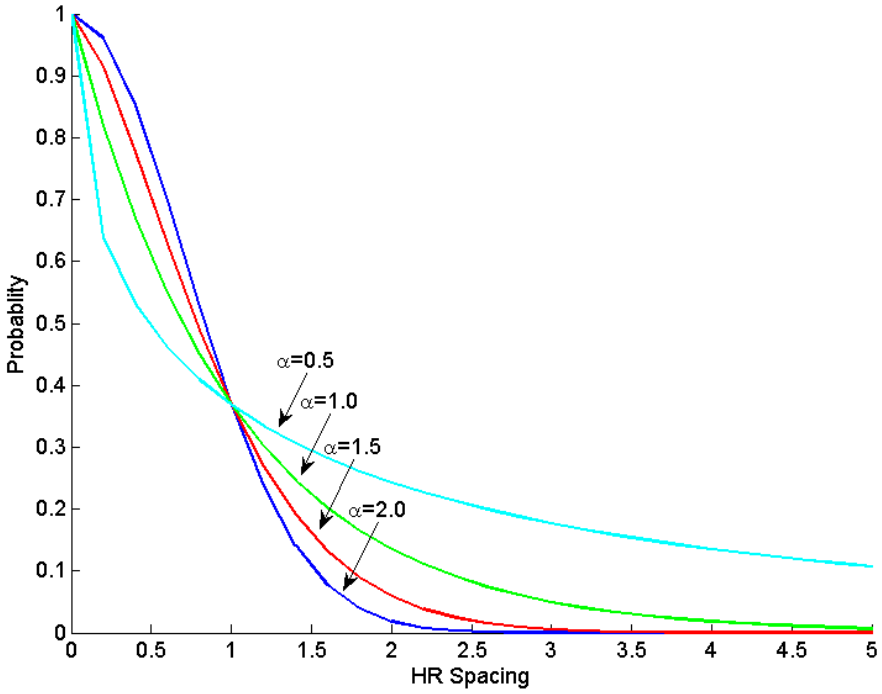

Figure 3.1 Characteristic functions of a stable distribution with γ=1.

In order to investigate whether model function (3.4) is better than model function (3.1) to model the intensity covariance between two HR pixels, a simulation was carried out to evaluate the modeling performance of the two models. In particular, a set of testing images shown in Appendix A were partitioned into a number of local regions to form a set of patch data for evaluation. With the evaluation data set, model functions (3.4) and (3.1) were then, respectively, used as the target model function to obtain the corresponding optimal model parameters using a regression analysis. Specifically, the following cost function was minimized in the optimization.

$$J = \sum_{k \in \Phi} \sum_{|\Delta i|,|\Delta j| \le \phi} \left(r_{xx(k)}(\Delta i, \Delta j) - \hat{r}_{xx(k)}(\Delta i, \Delta j) \right)^2 \quad \text{for all patch } k \qquad (3.5)$$

where $r_{xx(k)}$ is the covariance matrix derived with (i) a particular target model function and (ii) the variance of the k^{th} patch in the evaluation data set Φ, and $\hat{r}_{xx(k)}$ is the covariance matrix computed with the real data in the patch. ϕ is the range of signal to be considered in the measure. For example, a 5×5 image block containing totally 25 pixels is involved in the computation when $\phi = 5$.

When model function (3.4) was used as the target model function, its optimized parameters α and γ were obtained by solving the following equations.

$$\begin{cases} \dfrac{\partial J}{\partial \alpha} = 0 \\ \dfrac{\partial J}{\partial \gamma} = 0 \end{cases} \qquad (3.6)$$

where

$$\frac{\partial J}{\partial \alpha} = \sum_{k} \sum_{|\Delta i|,|\Delta j| \le 5} 2\left(r_{xx(k)}(\Delta i, \Delta j) - \hat{r}_{xx(k)}(\Delta i, \Delta j)\right) \frac{\partial}{\partial \alpha}\left(r_{xx(k)}(\Delta i, \Delta j)\right)$$

$$= -\sum_{k} \sum_{|\Delta i|,|\Delta j| \le 5} \left(2\left(r_{xx(k)}(\Delta i, \Delta j) - \hat{r}_{xx(k)}(\Delta i, \Delta j)\right) \cdot r_{xx(k)}(\Delta i, \Delta j) \right. \\ \left. \cdot \gamma(\Delta i^2 + \Delta j^2)^{\alpha/2} \cdot \ln(\sqrt{\Delta i^2 + \Delta j^2})\right) \tag{3.7}$$

and

$$\frac{\partial J}{\partial \gamma} = \sum_{k} \sum_{|\Delta i|,|\Delta j| \le 5} 2\left(r_{xx(k)}(\Delta i, \Delta j) - \hat{r}_{xx(k)}(\Delta i, \Delta j)\right) \frac{\partial}{\partial \gamma}\left(r_{xx(k)}(\Delta i, \Delta j)\right)$$

$$= -\sum_{k} \sum_{|\Delta i|,|\Delta j| \le 5} 2\left(r_{xx(k)}(\Delta i, \Delta j) - \hat{r}_{xx(k)}(\Delta i, \Delta j)\right) \cdot r_{xx(k)}(\Delta i, \Delta j) \cdot \left((\Delta i^2 + \Delta j^2)^{\alpha/2}\right)$$

(3.8)

It is not easy to solve eqns. (3.7) and (3.8) directly and hence the gradient descent method was exploited to solve the equations iteratively as follows.

$$\begin{cases} \alpha_t = \alpha_{t-1} - \lambda \cdot \left.\dfrac{\partial J}{\partial \alpha}\right|_{\alpha=\alpha_{t-1}} \\ \gamma_t = \gamma_{t-1} - \lambda \cdot \left.\dfrac{\partial J}{\partial \gamma}\right|_{\gamma=\gamma_{t-1}} \end{cases} \tag{3.9}$$

where α_t and γ_t, respectively, denote the estimates of α and γ obtained at the t^{th} iteration. Parameter λ is a positive step size which controls the speed of convergence. In our evaluation study, λ is empirically chosen to be 0.1. The initial estimate of α and γ are α_0=2 and γ_0=1 respectively, which makes the initial estimate of the model function as the conventional Gaussian function. This makes sure that the final estimate of the model function obtained with the gradient descent method does not deviate from the conventional Gaussian function too much and at the same time it is locally optimal.

When model function (3.1) was used as the target model function, its optimized parameter ρ was obtained by solving

$$\frac{\partial J}{\partial \rho} = 0 \tag{3.10}$$

where

$$\frac{\partial J}{\partial \rho} = \sum_{k} \sum_{|\Delta i|,|\Delta j| \le 5} 2\left(r_{xx(k)}(\Delta i, \Delta j) - \hat{r}_{xx(k)}(\Delta i, \Delta j)\right) \frac{\partial}{\partial \rho}\left(r_{xx(k)}(\Delta i, \Delta j)\right)$$

$$= \sum_{k} \sum_{|\Delta i|,|\Delta j| \le 5} 2\left(r_{xx(k)}(\Delta i, \Delta j) - \hat{r}_{xx(k)}(\Delta i, \Delta j)\right) \cdot r_{xx(k)}(\Delta i, \Delta j) \cdot \left(\sqrt{\Delta i^2 + \Delta j^2} \,/\, \rho\right) \tag{3.11}$$

Again, it is not easy to solve eqn. (3.11) directly and the gradient descent method was exploited to solve the equations iteratively as follows.

$$\rho_t = \rho_{t-1} - \lambda \cdot \left.\frac{\partial J}{\partial \rho}\right|_{\rho=\rho_{t-1}} \tag{3.12}$$

where ρ_t denotes the estimate of ρ obtained at the t^{th} iteration. The initial estimate of ρ is ρ_0=0.95 which is tentatively picked and it does not affect the final optimal estimate in our study.

From the regression results, it was found that the optimal model parameter value for model (3.1) was ρ=0.9 while the optimal model parameters for model (3.4) were α=1.4 and γ=0.46. Table 3.1 shows the cost associated with the two optimized models for the testing data. The cost is computed based on the cost function (3.5). The result shown in the table justifies that the model based on function (3.4) is better as compared with the model based on function (3.1) to describe the local intensity covariance between two pixels in an image having the characteristics similar to the images shown in Appendix A.

$r_{xx}(\Delta i, \Delta j)$ model	$\sigma_x^2 \exp\left(-0.46(\Delta i^2 + \Delta j^2)^{0.7}\right)$	$\sigma_x^2 (0.9)^{\sqrt{\Delta i^2 + \Delta j^2}}$
Cost in terms of J	0.0624	1.0244

Table 3.1 Fitting performance of different covariance models of pixel intensity

values in a local region of an image based on a set of testing images.

Since model function (3.4) is better to describe the intensity covariance between two pixels in an image, hereafter we will use it as the default model function framework instead of the one proposed in AWFc[Hardie07] in our subsequent study unless it is specified otherwise.

3.3 Classified intensity covariance models

AWFc exploits a covariance model which adapts to the local sample variance only. It does not take the edge characteristics into account. In practice, pixels are more correlated in a non-edge region than an edge region as an edge breaks the correlation between the pixels in different sides of the edge. In view of this, a simple trick is proposed to improve the model in this section. In particular, by making use of a simple edge-sensing detector, we classify a local patch as either an edge patch or not, and then apply a corresponding covariance model to derive the correlation between the HR pixels in the patch.

The classification of patches is implemented with a classifier referred to as local context classifier (LCC) in this work. First of all, the LR image whose grid aligns with the grid of the target HR image is selected to be the reference LR image. The intensity gradient magnitude of the reference image at each pixel is estimated by convolving the image with a Sobel operator. As a result, a gradient map of the image is formed. A binary edge map is then obtained by thresholding the resultant gradient map. Accordingly, based on the portion of the edge map associated with a particular local patch, any pixel in the patch is classified as either an edge pixel or not. If more than half of the pixels in a patch are edge pixels, the patch is considered as an edge patch or else it is not.

For each type of patches, a dedicated intensity covariance model is required. A set of testing images shown in Appendix B were partitioned into a number of local

regions to form a set of patch data for parameter evaluation. All patches in the set were classified with LCC. During the classification, the original images were all treated as LR images.

To determine the optimal α and γ for edge patches, all edge patches in the set were collected to form a subset, which is denoted as Φ_e, and the following cost function was minimized with respect to α and γ respectively.

$$J = \sum_{k \in \Phi_e} \sum_{|\Delta i|,|\Delta j| \le 5} \left(\sigma^2_{x(k)} \exp\left(-\gamma (\Delta i^2 + \Delta j^2)^{\alpha/2} \right) - \hat{r}_{xx(k)}(\Delta i, \Delta j) \right)^2 \tag{3.14}$$

where k is the index value of the k^{th} patch in set Φ_e, $\sigma^2_{x(k)}$ is the intensity variance of the patch, and $\hat{r}_{xx(k)}$ is the covariance matrix computed with the real data in the patch. It was found that the optimal model parameter values for edge patches are α=1.454 and γ=0.450.

Similarly, the optimal model parameter values for non-edge patches were also determined with all non-edge patches in the evaluation set. In particular, they were found to be α=1.12 and γ=0.474. One can see that the α value for non-edge patches is smaller than that for edge patches. This implies that there is a stronger correlation between two pixels which are considerably far apart in a non-edge region.

After all, the two local intensity covariance models for different regions are given as

$$r_{xx}(\Delta i, \Delta j) = \begin{cases} \sigma_x^2 \exp\left(-0.45(\Delta i^2 + \Delta j^2)^{0.727} \right) & \textit{for edge region} \\ \sigma_x^2 \exp\left(-0.474(\Delta i^2 + \Delta j^2)^{0.560} \right) & \textit{for non-edge region} \end{cases} \tag{3.15}$$

where σ_x^2 is the local intensity variance of the unknown HR image. Figure 3.2 shows the intensity covariance models used in AWFc and the ones used in our

proposed algorithm for comparison. They are all normalized such that $r_{xx}(0,0)=1$.

In practice, σ_x^2 has to be estimated with the LR pixels in a particular local region. In our realization, σ_x^2 is estimated as

$$\sigma_x^2 = \max\left\{(\sigma_y^2 - \sigma_n^2)/C, 0\right\} \tag{3.16}$$

where σ_y^2 is the intensity variance of all LR pixels registered in the region, σ_n^2 is the local noise variance and

$$C = \iint e^{-\gamma(\sqrt{i^2+j^2})^{\alpha}} \cdot (b(i,j) * b(-i,-j)) \cdot di \cdot dj \tag{3.17}$$

where $b(i,j)$ is the blurring function discussed in Section 2.4. By following the steps detailed in Section 2.4, the weights of all LR pixels used to estimate a HR pixel in the region can be determined and, accordingly, the HR image can be obtained by adaptive Wiener filtering.

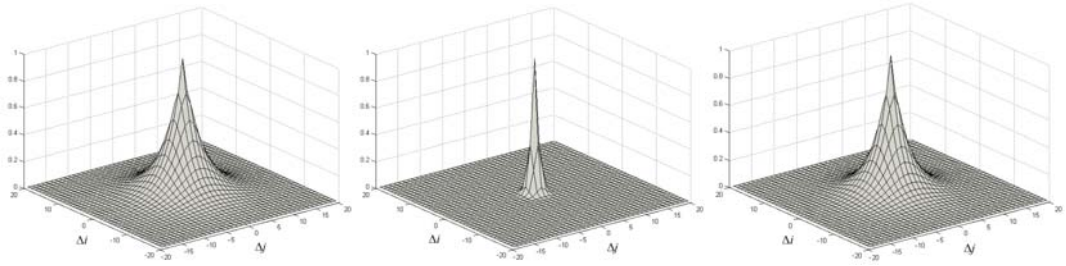

(a) (b) (c)

Figure 3.2 Normalized local intensity covariance models of HR patches: (a) AWFc[Hardie07] (b) ours for edge region, and (c) ours for non-edge region

The modification presented in this chapter to AWFc results in a new algorithm. This algorithm classifies a local region to be either an edge region or not and then selects a corresponding spatial intensity covariance model to adaptively adjust the weights of the LR pixels when estimating the HR pixels in the region. Hereafter, this algorithm is referred to as AWFcs for reference.

3.4 Simulation results

Simulations were carried out to evaluate the improvement of the proposed algorithm with respect to AWFc and some other super-resolution image reconstruction methods. A set of twenty 8-bit gray level aerial images shown in Appendix A were used as original HR images in the simulation. All of them are of original size 500×500 pixels. For each one of them, a sequence of 10 LR images was generated as follows.

First of all, a sequence of real value displacement vectors was randomly generated in a way that the value of each of their elements was bounded by ±2. The HR image was then translationally shifted by sub-pixel spacing using bicubic interpolation, blurred with a Gaussian filter of size 5×5, down-sampled by 5 in both horizontal and vertical directions, and finally corrupted with additive zero-mean random noise of variance σ_n^2. The translational shift for the k^{th} image in the sequence was set to be the accumulated sum of the first k-1 aforementioned displacement vectors. In the simulation, the original HR images were estimated with their corresponding LR sequences. In other words, the ratio of the target resolution of the reconstructed HR image to the resolution of a LR image for each dimension is 5. A sliding window of size 15×15 pixels moves over the HR grid to reconstruct the 5×5 HR pixels in the center region of the window. The initial sub-pixel registration step was carried out with the algorithm proposed in [Keren88].

Tables 3.2 and 3.3 show the performance achieved with different super-resolution image reconstruction algorithms in terms of *PSNR* under noise conditions σ_n^2=25 and σ_n^2=50 respectively. In particular, *PSNR* is defined as

$$PSNR = 10 \cdot \log_{10} \frac{255^2}{\frac{1}{N_0} \sum_{(i,j)} (x(i,j) - \hat{x}(i,j))^2} \text{ in dB} \qquad (3.18)$$

where x and $\hat{x}$ are, respectively, the original HR image and its estimate, and N_0 is the total number of image pixels involved in the comparison.

Noise		σ_n^2=25						
Image		Bicubic	Elad97	Farsiu04	AWFc	Pham06	AWFcs	AWFcs*
PSNR (dB)	1	19.00	20.49	21.30	25.42	25.42	26.02	25.59
	2	18.66	20.15	20.93	24.80	24.77	25.35	25.06
	3	21.01	23.32	23.99	29.24	29.25	29.74	29.27
	4	17.62	19.35	18.24	22.49	22.50	22.98	22.68
	5	18.93	20.92	21.21	25.08	25.07	25.44	25.13
	6	22.42	22.79	23.98	27.64	27.72	27.47	27.52
	7	17.86	18.81	19.88	22.34	22.35	22.51	22.46
	8	17.95	19.95	20.66	25.28	25.29	25.99	25.44
	9	17.28	18.83	19.53	23.63	23.64	24.56	23.54
	10	17.71	18.97	19.87	24.17	24.12	24.53	24.14
	11	16.60	17.92	18.72	22.76	22.75	22.93	22.53
	12	18.22	20.41	21.02	26.17	26.16	27.03	25.21
	13	18.17	20.47	21.13	26.65	26.66	27.54	26.86
	14	19.34	20.95	21.83	25.94	25.95	26.63	25.31
	15	18.65	20.11	20.89	24.89	24.89	25.08	25.14
	16	17.90	19.70	20.32	23.84	23.85	24.52	24.17
	17	18.48	19.71	20.54	23.80	23.79	24.16	23.98
	18	20.11	21.81	22.61	26.32	26.31	26.42	26.63
	19	17.82	19.16	20.00	23.41	23.43	23.86	23.61
	20	17.29	18.75	19.47	23.25	23.23	23.11	23.15
	Average:	18.55	20.13	20.81	24.86	24.86	25.29	24.87
Average Time:		0.02s	15.74s	45.16s	25.15s	29.21s	25.54s	25.80s

Table 3.2 *PSNR* performance (in dB) and computation time of various super-resolution image reconstruction algorithms under noise condition $\sigma_n^2 = 25$

Noise		σ_n^2=50						
Image		Bicubic	Elad97	Farsiu04	AWFc	Pham06	AWFcs	AWFcs*
PSNR (dB)	1	18.94	20.33	21.29	25.11	25.12	25.67	25.25
	2	18.61	20.00	20.91	24.59	24.57	25.07	24.68
	3	20.92	23.03	23.92	28.71	28.19	28.96	28.50
	4	17.58	18.16	19.38	22.25	22.28	22.75	22.46
	5	18.86	20.34	21.21	24.86	24.81	25.16	24.69
	6	22.27	22.55	23.96	27.52	27.08	27.10	26.22
	7	17.80	18.73	19.88	22.21	22.18	22.02	22.27
	8	17.90	19.82	20.64	25.05	25.02	25.66	24.84
	9	17.24	18.85	19.65	23.13	23.42	24.31	23.12
	10	17.66	18.86	19.86	23.91	23.93	24.27	23.67
	11	16.57	17.84	18.71	22.54	22.57	23.02	22.21
	12	18.18	20.30	21.02	25.78	25.85	26.64	24.50
	13	18.10	20.32	21.12	26.10	26.32	27.01	26.33
	14	19.29	20.80	21.79	25.69	25.66	25.87	23.97
	15	18.58	20.30	21.08	24.74	24.69	24.89	24.83
	16	17.84	19.59	20.00	23.64	23.69	24.26	23.79
	17	18.42	19.59	20.54	23.58	23.58	23.13	23.58
	18	20.04	21.62	22.60	26.05	26.12	26.69	26.16
	19	17.78	19.06	20.00	23.24	23.20	22.91	23.29
	20	17.26	18.65	19.48	23.04	23.05	22.46	22.80
	Average:	18.49	19.94	20.85	24.59	24.57	24.89	24.36
Average Time:		0.02s	15.74s	45.16s	25.15s	29.21s	25.54s	25.80s

Table 3.3 *PSNR* performance (in dB) and computation time of various super-resolution image reconstruction algorithms under noise condition $\sigma_n^2 = 50$.

In AWFcs, the two covariance models exploited for regions of different nature are derived based on model function (3.4). In fact, the two models can also be derived based on model function (3.1). In our simulation, we also derived two optimized models based on model function (3.1) with the images shown in Appendix B and used them instead in AWFcs to realize super-resolution image reconstruction. This version

of AWFcs is referred to as AWFcs* and its performance is also shown in Tables 3.2 and 3.3 for comparison. One can see that AWFcs* is inferior to AWFcs. Once again, it verifies that function (3.4) is better than function (3.1) in modeling the local intensity covariance of an image.

Noise		σ_n^2=100						
Image		Bicubic	Elad97	Farsiu04	AWFc	Pham06	AWFcs	AWFcs*
PSNR (dB)	1	18.82	20.05	21.26	23.99	23.93	24.97	24.70
	2	18.46	19.76	20.89	24.23	24.20	24.30	24.03
	3	20.73	22.53	23.84	27.14	27.18	27.80	27.78
	4	17.49	17.98	19.34	21.93	22.02	22.34	22.12
	5	18.75	20.03	21.17	24.41	24.40	23.95	24.12
	6	22.00	22.23	24.10	26.84	26.99	26.43	25.06
	7	17.73	18.50	19.84	21.91	21.94	21.96	21.95
	8	17.81	19.57	20.62	24.30	24.67	25.00	24.39
	9	17.16	18.69	19.67	23.08	23.03	22.77	23.29
	10	17.58	18.67	19.85	23.56	23.17	23.18	22.85
	11	16.51	17.71	18.72	22.26	22.19	21.81	21.84
	12	18.09	20.07	21.00	25.30	25.30	22.98	23.64
	13	17.99	20.02	21.10	25.17	25.10	26.19	25.76
	14	19.15	20.52	21.78	25.25	25.23	23.82	22.44
	15	18.48	20.02	21.06	24.37	24.36	24.43	24.34
	16	17.75	19.35	20.30	23.37	23.42	23.19	23.38
	17	18.33	19.37	20.54	23.28	23.27	23.17	23.27
	18	19.89	21.28	22.58	25.78	25.77	25.29	25.15
	19	17.68	19.62	19.66	22.21	22.29	22.97	22.34
	20	17.20	18.50	19.47	22.17	22.10	22.13	22.19
	Average:	18.38	19.72	20.84	24.03	24.03	23.93	23.73
Average Time:		0.02s	15.74s	45.16s	25.15s	29.21s	25.54s	25.80s

Table 3.4 *PSNR* performance (in dB) and computation time of various super-resolution image reconstruction algorithms under noise condition $\sigma_n^2 = 100$.

The Table 3.4 shows the performance of various algorithms under noise condition σ_n^2=100. It is found that AWFcs is more sensitive than AWFc to the noise.

When noise condition is very poor, its performance is even lower than that of AWFc.

Figures 3.3-3.5 show parts of the simulation results of different super-resolution image reconstruction algorithms for visual comparison. The input LR sequences are corrupted with random Gaussian noise of σ_n^2=50. In particular, Figures 3.3(a), 3.4(a) and 3.5(a) show the first LR frames of the LR sequences. They are interpolated by duplication for display. In general, the proposed algorithm provides sharper and more robust interpolation results than the other evaluated algorithms. By taking the classification result into account when deriving the covariance model among pixels, the proposed algorithm handles regions of different nature separately and provides better processing results. This can be verified from the outputs shown in Figures 3.3(f), 3.4(f) and 3.5(f). The algorithms were also evaluated with the real LR images shown in Appendix C to investigate their performance in real situation. Figure 3.6 shows the reconstruction results of the 5th image. The zooming factor is 5. Similar observations can be found.

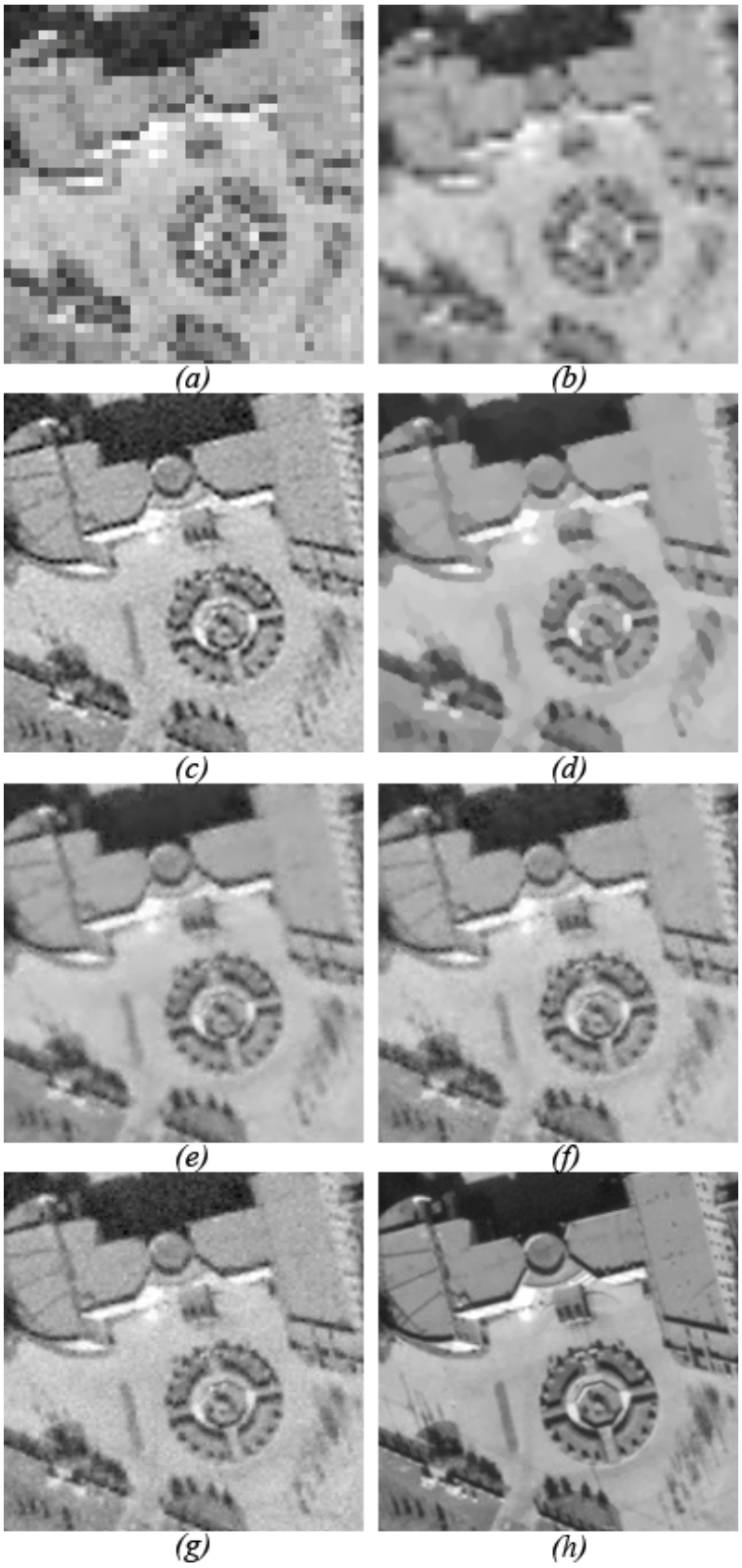

Figure 3.3 Parts of the super-resolution image reconstruction results of Image 3: (a) interpolation by duplication, (b) Bicubic, (c) Elad97, (d) Farsiu04, (e) AWFc, (f) AWFcs, (g) Pham06 and (h) the original

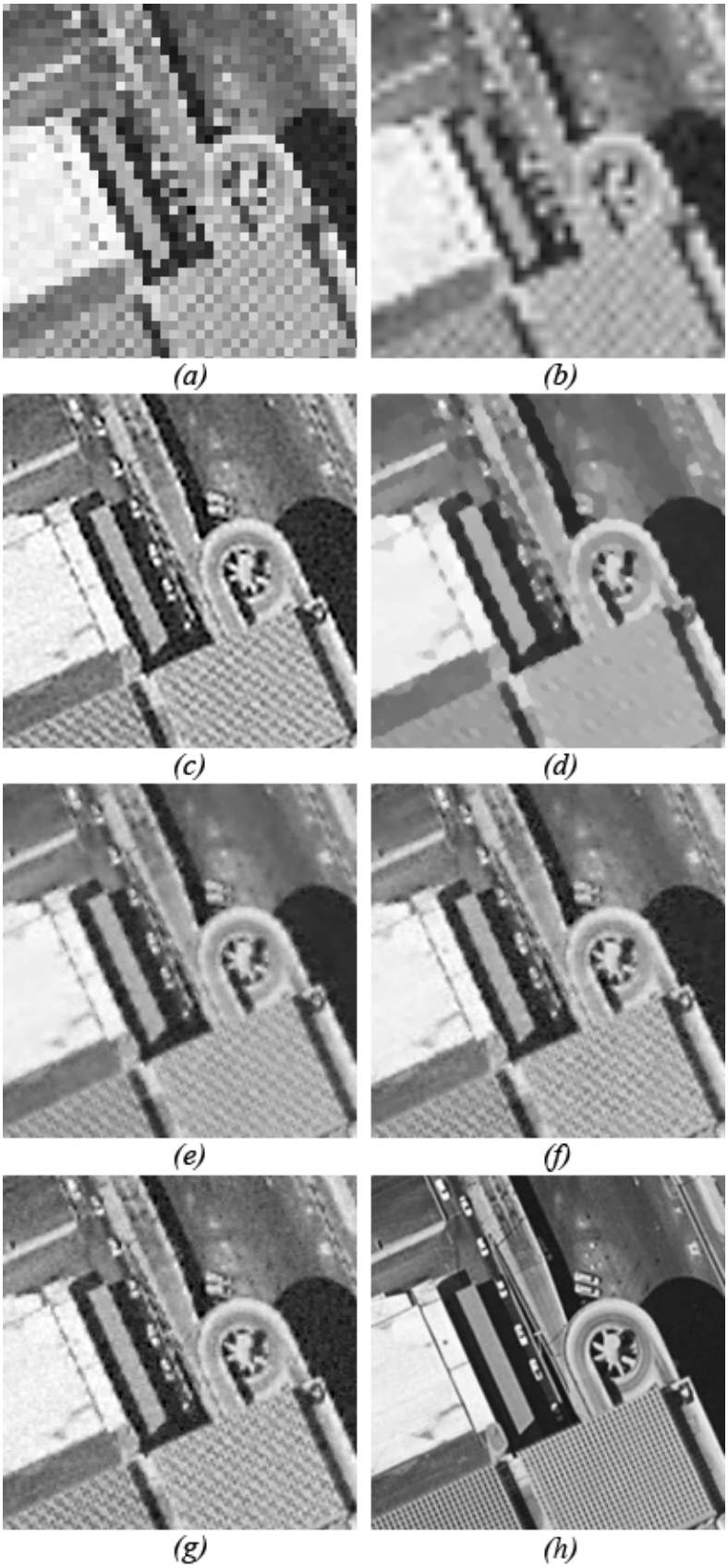

Figure 3.4 Parts of the super-resolution image reconstruction results of Image 7: (a) interpolation by duplication, (b) Bicubic, (c) Elad97, (d) Farsiu04, (e) AWFc, (f) AWFcs, (g) Pham06 and (h) the original

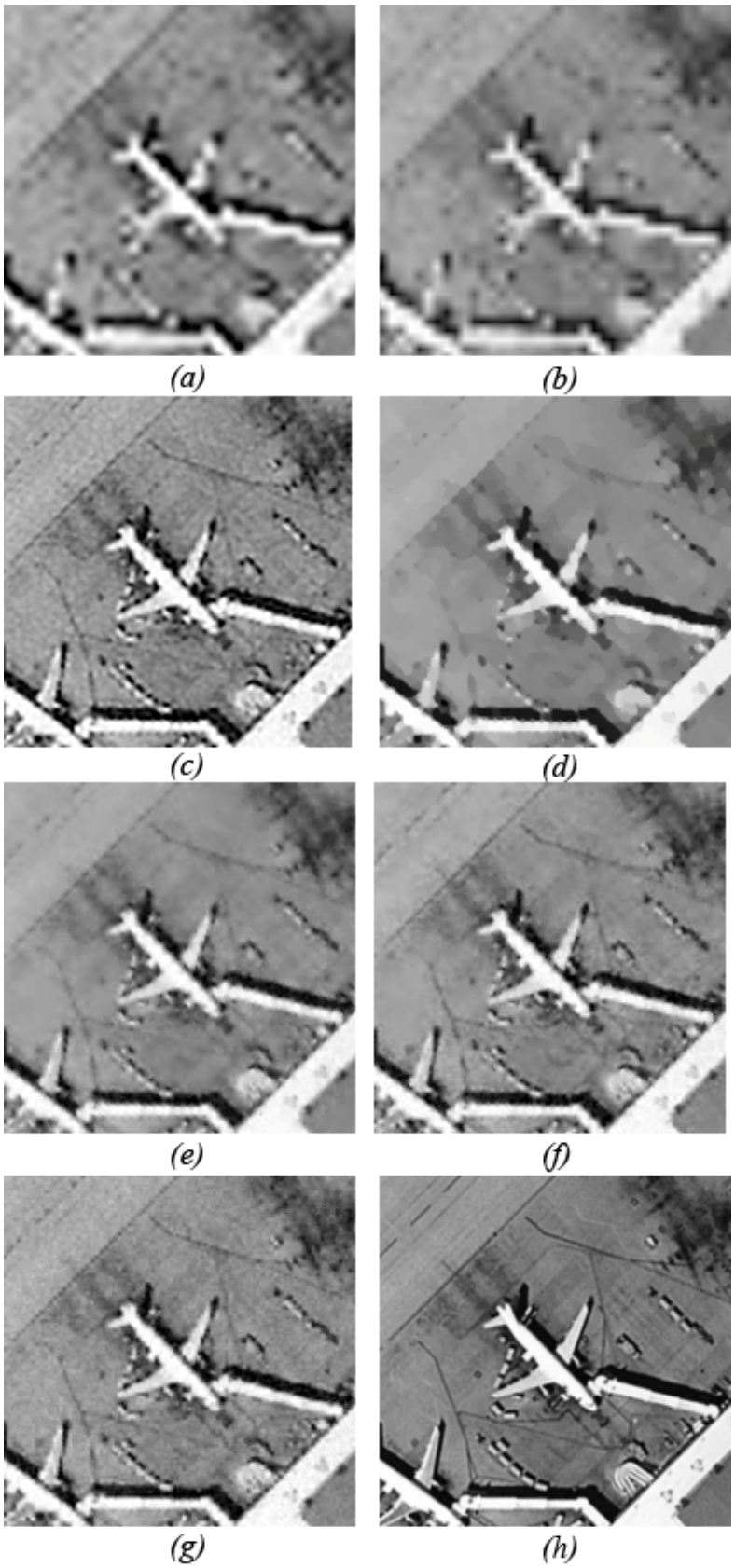

Figure 3.5 Parts of the super-resolution image reconstruction results of Image 8: (a) interpolation by duplication, (b) Bicubic, (c) Elad97, (d) Farsiu04, (e) AWFc, (f) AWFcs, (g) Pham06 and (h) the original

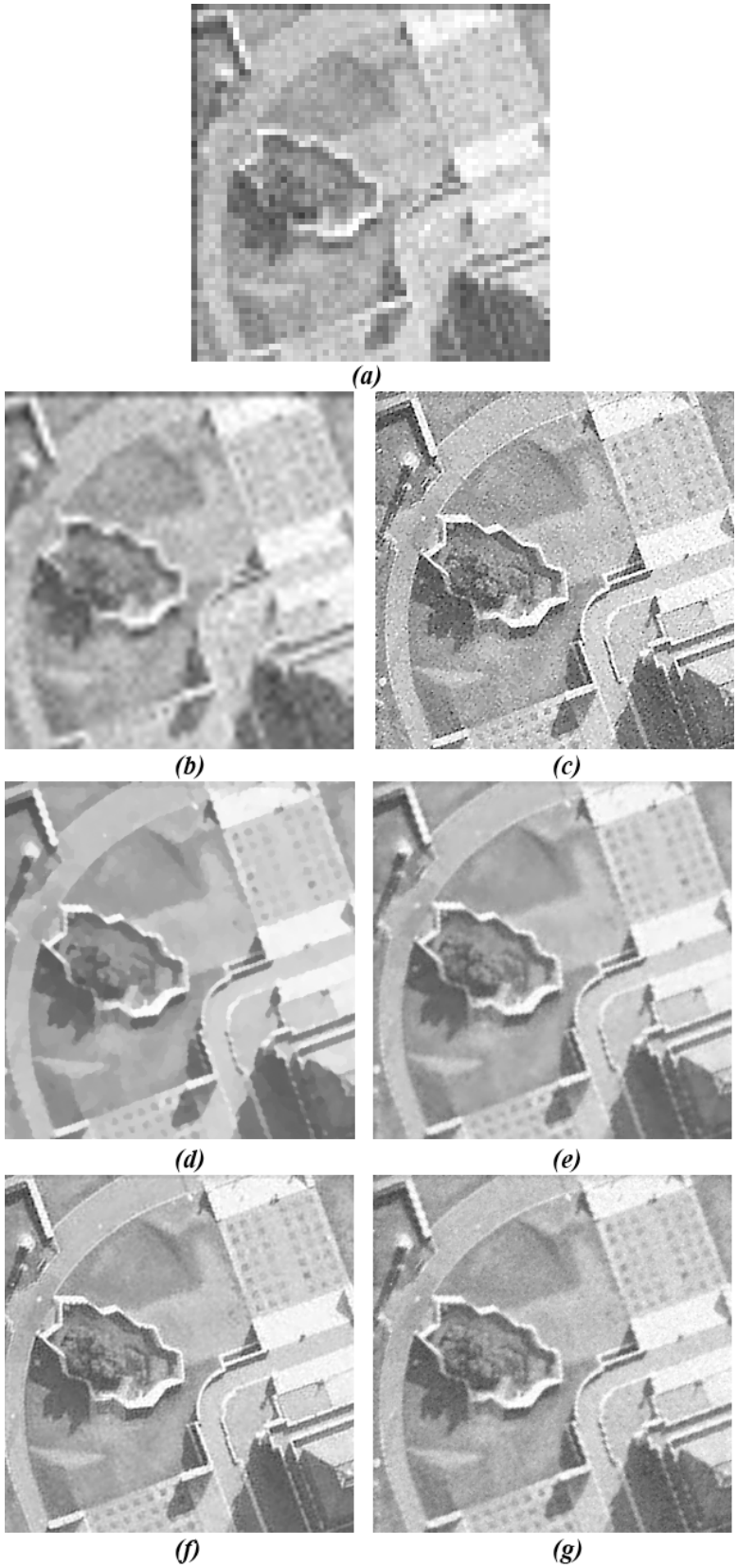

Figure 3.6 Parts of the super-resolution image reconstruction results obtained with real captured images: (a) interpolation by duplication, (b)Bicubic, (c) Elad97, (d) Farsiu04, (e) AWFc, (f) AWFcs and (g) Pham06

3.5 Summary

The proposed modification to AWFc [Hardie07] classifies image regions and accordingly adapts the covariance model of HR pixels to reflect the real situation when determining the weights of the involved LR pixels to estimate a HR pixel. As a consequence, the improved algorithm adapts the estimation of HR pixels to both the local sample variance and the local edge characteristics. Simulation results show that the modification improves the super-resolution image reconstruction performance both objectively and subjectively.

However, this binary classification scheme may still be too simple to handle regions with various contexts well. For example, the edge orientation in an edge region should also affect the intensity covariance model in the region. In the following chapter, this issue is addressed and a solution is proposed accordingly to take this into account.

Chapter 4

ADAPTIVE WIENER FILTERING WITH A DIRECTIONAL INTENSITY COVARIANCE MODEL

4.1 Introduction

As shown in Chapter 3, the success of the simple trick exploited in our first attempt to improve the performance of AWFc ***confirms the direction*** of improvement. As a matter of fact, the idea can be further extended to improve the intensity covariance model. Obviously, pixels along an edge should be more correlated than those pixels in different sides of the edge. As a result, the covariance model function should be anisotropic according to the edge orientation in a local region. In our second attempt, we evaluate the sample variances along various directions in a local region and, based on the evaluation result, adjust the shape of covariance model function. By doing so, the orientation of the covariance model function and the extent of its asymmetricity are fully adaptive to the local characteristics. Unlike the approach adopted in our first attempt, no explicit region classification is required.

This chapter is organized as follows. In section 4.2, an adaptive directional intensity covariance model is introduced and its difference to the conventional isotropic covariance model is contrasted. Replacing the original covariance model

used in AWFc[Hardie07] with this directional intensity covariance model results in a new version of adaptive Wiener filtering algorithm for super-resolution image reconstruction. In Section 4.3, some simulation results are presented for performance evaluation. Finally, a brief summary is given in the last section.

4.2 Directional covariance model

As shown in eqns. (3.1) and (3.4), the covariance model exploited in AWFc and those exploited in AWFcs are all isotropic models. In practice, covariances among samples in a local region are probably not isotropic due to the presence of edges or texture. Hence, a directional anisotropic covariance model would be better to describe the actual situation. The subsequent question is how to estimate the edge direction and the anisotropic characteristic in a local region.

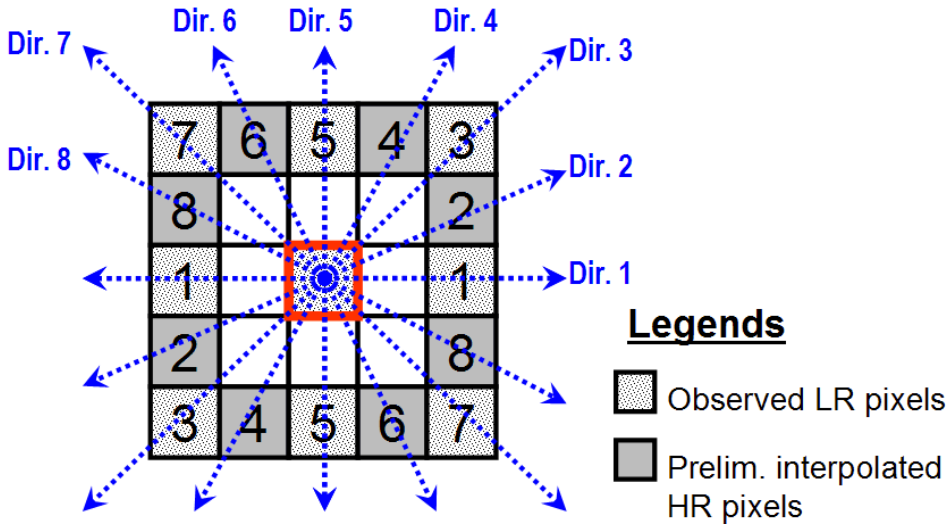

Figure 4.1 A preliminarily interpolated 5x5 image patch for estimating local anisotropic characteristic

Here, we propose to initially interpolate the observed signal to a higher resolution before estimating the direction and anisotropic characteristic. As an example, when the enlargement factor equals 2, every 3×3 local patch in the LR

image is first preliminarily interpolated to a 5x5 HR image patch by bicubic interpolation before estimating the anisotropic characteristic of the region. Figure 4.1 shows the pixel arrangement of the enlarged image patch with its center served as the center of the interested region.

After the interpolation, the mean square gradient value along each of the 8 possible directions shown in Figure 4.1 is estimated by using the pair of pixels marked with the corresponding direction index value and the center pixel. For instance, for direction 3, the corresponding mean square gradient value is computed as

$$\sigma_3^2 = \sum_{m=\pm 2} \left(g(i_o + m, j_o + m) - g(i_o, j_o) \right)^2 \tag{4.1}$$

where $g(i,j)$ is the known (either by estimation or observation) sample value at position (i,j) of the 5x5 HR image patch, and (i_o, j_o) are the coordinates of the center.

The direction t that provides the minimum mean square gradient value, denoted as t_{major}, is regarded as the major axis of the correlation model while its perpendicular direction is the minor axis denoted as t_{minor}. In formulation, we have

$$t_{major} = \arg \min_{t=1,2...8} \{\sigma_t^2\} \tag{4.2}$$

where σ_t^2 is the mean square gradient value along direction t.

The eccentricity ratio defined as

$$\kappa = \sigma_{t_{minor}}^2 / \sigma_{t_{major}}^2 \tag{4.3}$$

is then used to describe the anisotropic characteristic of the region. To avoid extreme values, clipping is used to bound the value of κ between 0 and 1.

With parameter κ, the proposed directional anisotropic covariance model is defined as

$$r_{xx}(\Delta i, \Delta j) = \sigma_x^2 e^{-(\gamma\sqrt{\kappa(\cos\theta\Delta i-\sin\theta\,\Delta j)^2+(\sin\theta\,\Delta i+\cos\theta\,\Delta j)^2})^{\alpha}} \qquad (4.4)$$

where θ is the angle from direction 1 to direction t_{major}.

By controlling κ, one can adjust the correlation model to be anisotropic for an edge region or isotropic for a smooth region adaptively according to the nature of the local region. Figure 4.2 shows the shapes of model function (4.4) of different values of κ when (α, γ)=(1.4, 0.46) and t_{major}=3. Here, (α, γ) is selected to be (1.4, 0.46) based on the simulation result presented in Section 3.2. In that study, all patches generated with the images shown in Appendix A were used without classification to derive the optimal values of α and γ. The optimization result is (α, γ)=(1.4, 0.46).

An empirical study was carried out to demonstrate the appropriateness of the anisotropic model proposed in this chapter in modeling the local spatial covariance of an image. In this study, the local intensity covariance of patches with various context were modeled with function (4.4) and function (3.4) respectively. The resultant models were than evaluated to see if they could reflect the reality.

Figure 4.3 shows a typical image and Figure 4.4(a) shows 4 marked regions of the image shown in Figure 4.1. The 4 regions are of different local spatial content. The intensity covariance between any pixel in a paricular region and the center pixel of the region is modeled with functions (3.4) and (4.4) respectively. Figure 4.4(b) and Figure 4.4(c), respectively, show the normalized contour plot of the two resultant models. One can see that the proposed family of anisotropic models is more appropriate than the isotropic models to describe the local intensity covariance of the regions.

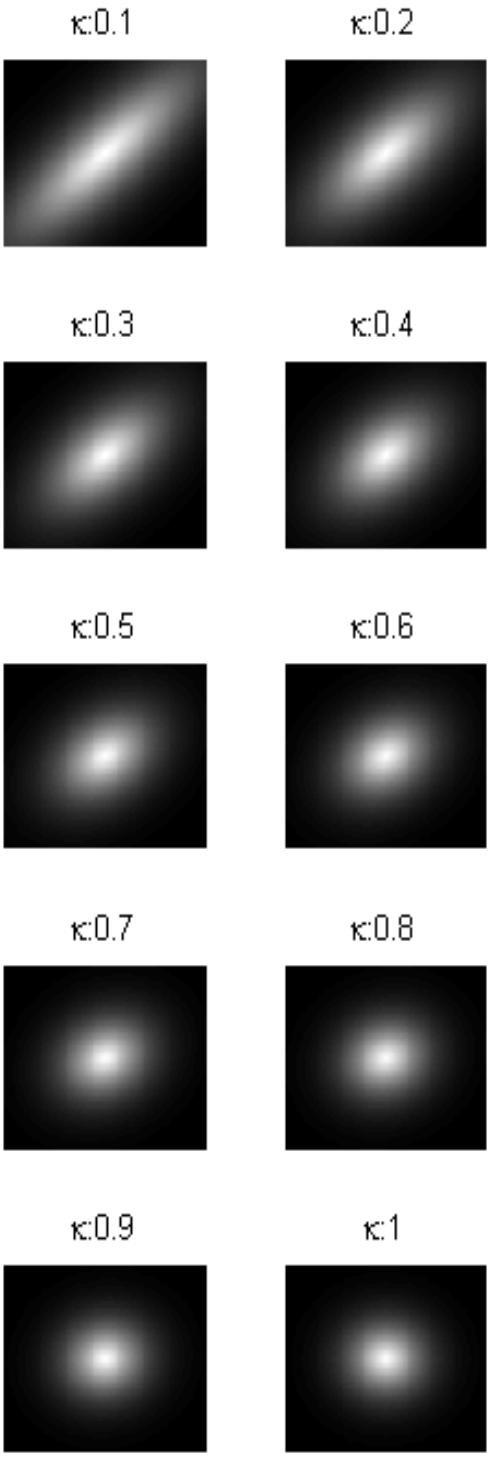

Figure 4.2 Normalized directional covariance model function with different κ

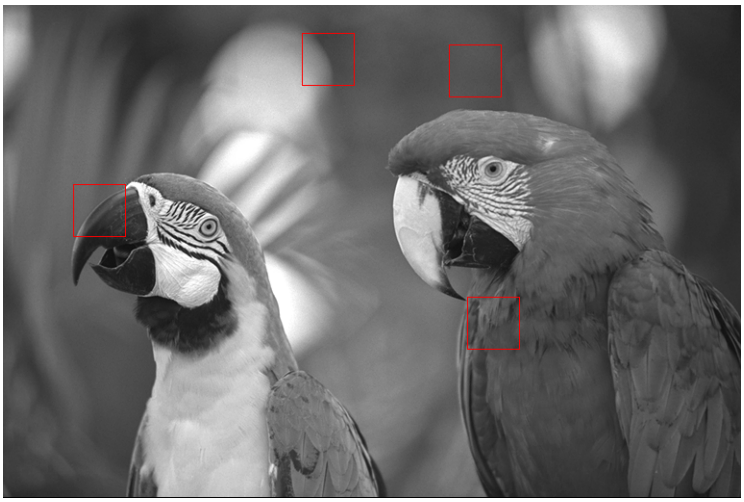

Figure 4.3 A typical image with four marked local regions

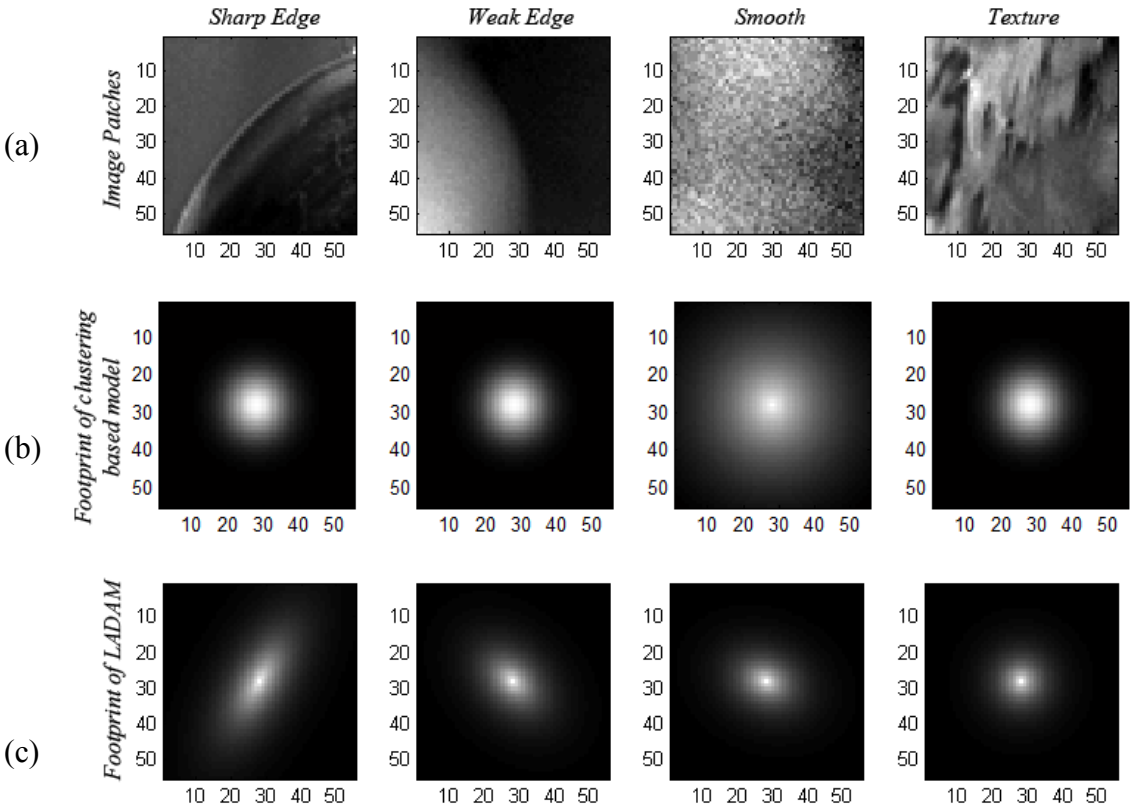

Figure 4.4 Covariance models derived for regions of different nature based on different approaches: (a) spatial content of local regions, (b) normalized isotropic model function derived based on function (3.4) and (c) normalized directional model function derived based on function (4.4)

As discussed in Section 2.5, the model used to describe the covariance between two HR pixels are critical to the performance of adaptive Wiener filtering in super –resolution image reconstruction. When directional covariance model function (4.4) is used instead of function (3.1) to model the local intensity covariance of an HR image, σ_x^2 is the local variance of the unknown HR image and it has to be estimated with the LR pixels in the local region. In our realization, σ_x^2 is estimated as

$$\sigma_x^2 = \max\left\{(\sigma_y^2 - \sigma_n^2)/C, 0\right\} \tag{4.5}$$

where σ_y^2 is the variance of all LR pixels registered in the region, σ_n^2 is the local noise variance and

$$C = \iint e^{-\gamma\left(\sqrt{\kappa(i\cos\theta - j\sin\theta)^2 + (i\sin\theta + j\cos\theta)^2}\right)^{\alpha}} \cdot (b(i,j) * b(-i,-j)) \cdot di \cdot dj \tag{4.6}$$

Function $b(i,j)$ is the blurring function discussed in Section 2.5. By following the steps detailed in Section 2.5, the weights of all LR pixels used to estimate a HR pixel in the region can be determined and, accordingly, the HR image can be obtained by adaptive Wiener filtering.

The modification presented in this chapter to AWFc results in a new algorithm. This algorithm estimates the edge or texture orientation in a local region and then adjusts the shape of the spatial intensity covariance model for the region. The weights of the LR pixels used to estimate the HR pixels in the region can hence be adaptively adjusted accordingly. As the local intensity model used in this algorithm can be anisotropic, this algorithm is referred to as AWFa for reference hereafter.

4.3 Simulation results

Simulations were carried out to evaluate the improvement of the proposed algorithm with respect to AWFc. The set of twenty 8-bit gray level aerial images shown in Appendix A were used as original HR images in the simulation. All of them are of original size 500×500 pixels. For each one of them, a sequence of 10 LR images was generated as follows.

First of all, a sequence of real value displacement vectors was randomly generated in a way that the value of each of their elements was bounded by ±2. The HR image was then translationally shifted by sub-pixel spacing using bicubic interpolation, blurred with a Gaussian filter of size 5×5, down-sampled by 5 in both horizontal and vertical directions, and finally corrupted with additive zero-mean random noise of variance σ_n^2. The translational shift for the k^{th} image in the sequence was set to be the accumulated sum of the first k-1 aforementioned displacement vectors.

The original HR images were estimated with their corresponding LR sequences in the simulation. The ratio of the target resolution of the reconstructed HR image to the resolution of a LR image for each dimension is 5. A sliding window of size 15×15 pixels moves over the HR grid to reconstruct the 5×5 HR pixels in the center region of the window. The initial sub-pixel registration step was carried out with the algorithm proposed in [Keren88].

Tables 4.1 and 4.2 show the performance achieved with different SR algorithms in terms of *PSNR* under noise conditions σ_n^2=25 and σ_n^2=50. One can see that the average performance of AWFa is better than other conventional super-resolution image reconstruction algorithms in terms of PSNR. As compared with AWFcs, on average there is a slight PSNR improvement.

Noise		σ_n^2 =25							
Image		Bicubic	Elad97	Farsi04	AWFc	Pham06	AWFcs	AWFa	AWFa*
PSNR (dB)	1	19.00	20.49	21.30	25.42	25.42	26.02	26.06	25.42
	2	18.66	20.15	20.93	24.80	24.77	25.35	25.44	24.86
	3	21.01	23.32	23.99	29.24	29.25	29.74	29.89	28.89
	4	17.62	19.35	18.24	22.49	22.50	22.98	23.08	22.59
	5	18.93	20.92	21.21	25.08	25.07	25.44	25.51	24.87
	6	22.42	22.79	23.98	27.64	27.72	27.47	28.18	27.19
	7	17.86	18.81	19.88	22.34	22.35	22.51	22.37	22.31
	8	17.95	19.95	20.66	25.28	25.29	25.99	26.27	25.30
	9	17.28	18.83	19.53	23.63	23.64	24.56	24.58	23.59
	10	17.71	18.97	19.87	24.17	24.12	24.53	24.57	23.97
	11	16.6.0	17.92	18.72	22.76	22.75	22.93	23.25	22.39
	12	18.22	20.41	21.02	26.17	26.16	27.03	27.25	24.98
	13	18.17	20.47	21.13	26.65	26.66	27.54	27.76	26.49
	14	19.34	20.95	21.83	25.94	25.95	26.63	26.94	25.23
	15	18.65	20.11	20.89	24.89	24.89	25.08	25.36	24.93
	16	17.90	19.70	20.32	23.84	23.85	24.52	24.53	23.75
	17	18.48	19.71	20.54	23.80	23.79	24.16	24.04	23.77
	18	20.11	21.81	22.61	26.32	26.31	26.42	27.06	26.47
	19	17.82	19.16	20.00	23.41	23.43	23.86	23.88	23.45
	20	17.29	18.75	19.47	23.25	23.23	23.11	23.66	22.91
	Average:	18.55	20.13	20.81	24.86	24.86	25.29	25.48	24.67
Average Time:		0.02s	15.74s	45.16s	25.15s	29.21s	25.54s	39.78s	39.75s

Table 4.1 *PSNR* performance (in dB) and computation time of various super-resolution image reconstruction algorithms under noise condition $\sigma_n^2 = 25.$

Noise		σ_n^2=50							
Image		Bicubic	Elad97	Farsiu04	AWFc	Pham06	AWFcs	AWFa	AWFa*
PSNR (dB)	1	18.94	20.33	21.29	25.11	25.12	25.67	25.66	25.05
	2	18.61	20.00	20.91	24.59	24.57	25.07	25.12	24.55
	3	20.92	23.03	23.92	28.71	28.19	28.96	29.08	28.25
	4	17.58	18.16	19.38	22.25	22.28	22.75	22.83	22.37
	5	18.86	20.34	21.21	24.86	24.81	25.16	25.17	24.52
	6	22.27	22.55	23.96	27.52	27.08	27.10	27.37	26.09
	7	17.80	18.73	19.88	22.21	22.18	22.02	22.18	22.09
	8	17.90	19.82	20.64	25.05	25.02	25.66	25.92	24.95
	9	17.24	18.85	19.65	23.13	23.42	24.31	24.27	23.29
	10	17.66	18.86	19.86	23.91	23.93	24.27	24.26	23.52
	11	16.57	17.84	18.71	22.54	22.57	23.02	23.02	22.09
	12	18.18	20.30	21.02	25.78	25.85	26.64	26.80	23.72
	13	18.10	20.32	21.12	26.10	26.32	27.01	27.16	26.03
	14	19.29	20.80	21.79	25.69	25.66	25.87	26.53	24.08
	15	18.58	20.30	21.08	24.74	24.69	24.89	25.02	24.67
	16	17.84	19.59	20.00	23.64	23.69	24.26	24.24	23.44
	17	18.42	19.59	20.54	23.58	23.58	23.13	23.78	23.49
	18	20.04	21.62	22.60	26.05	26.12	26.69	26.68	25.84
	19	17.78	19.06	20.00	23.24	23.20	22.91	23.31	23.17
	20	17.26	18.65	19.48	23.04	23.05	22.46	23.42	22.43
	Average:	18.49	19.94	20.85	24.59	24.57	24.89	25.09	24.18
Average Time:		0.02s	15.74s	45.16s	25.15s	29.21s	25.54s	39.78s	39.75s

Table 4.2 *PSNR* performance (in dB) and computation time of various super-resolution image reconstruction algorithms under noise condition $\sigma_n^2 = 50$.

Noise	σ_n^2=100							
Image	Bicubic	Elad97	Farsiu04	AWFc	Pham06	AWFcs	AWFa	AWFa*
1	18.82	20.05	21.26	23.99	23.93	24.97	24.97	24.46
2	18.46	19.76	20.89	24.23	24.20	24.30	24.53	24.10
3	20.73	22.53	23.84	27.14	27.18	27.80	28.15	27.35
4	17.49	17.98	19.34	21.93	22.02	22.34	22.22	22.01
5	18.75	20.03	21.17	24.41	24.40	23.95	23.85	23.89
6	22.00	22.23	24.10	26.84	26.99	26.43	25.64	24.85
7	17.73	18.50	19.84	21.91	21.94	21.96	21.72	21.86
8	17.81	19.57	20.62	24.30	24.67	25.00	25.21	24.14
9	17.16	18.69	19.67	23.08	23.03	22.77	23.15	22.38
10	17.58	18.67	19.85	23.56	23.17	23.18	23.32	22.84
11	16.51	17.71	18.72	22.26	22.19	21.81	21.56	21.57
12	18.09	20.07	21.00	25.30	25.30	22.98	22.92	22.61
13	17.99	20.02	21.10	25.17	25.10	26.19	26.29	25.44
14	19.15	20.52	21.78	25.25	25.23	23.82	23.86	22.60
15	18.48	20.02	21.06	24.37	24.36	24.43	24.28	23.95
16	17.75	19.35	20.30	23.37	23.42	23.19	23.32	23.01
17	18.33	19.37	20.54	23.28	23.27	23.17	22.88	23.02
18	19.89	21.28	22.58	25.78	25.77	25.29	25.27	24.51
19	17.68	19.62	19.66	22.21	22.29	22.97	22.86	22.42
20	17.20	18.50	19.47	22.17	22.10	22.13	21.72	21.91
Average:	18.38	19.72	20.84	24.03	24.03	23.93	23.89	23.45
Time:	0.02	15.74	45.16	25.15	29.21	25.54	39.78	39.75

Table 4.3 *PSNR* performance (in dB) of various super-resolution image reconstruction algorithms under noise condition σ_n^2 = 100.

Table 4.3 shows the performance of various algorithms under noise condition σ_n^2=50. Like AWFcs, AWFa is sensitive to noise when the noise condition is poor, the estimation of edge direction is not reliable and hence it results in a inaccurate covariance model. In such a case, AWFa is even poorer than AWFc.

Figures 4.5-4.7 show parts of the simulation results of different super-resolution image reconstruction algorithms for visual comparison. The input LR sequences are corrupted with random Gaussian noise of σ_n^2=50. In particular, Figures 4.5(a), 4.6(a) and 4.7(a) show the first LR frames of the LR sequences. They are interpolated by duplication for display. In general, the proposed algorithm provides sharper and more robust interpolation results than the other evaluated algorithms. By taking the edge and texture orientation in a local region into account when deriving the intensity covariance model among pixels, the proposed algorithm handles regions of different nature separately and provides better processing results. This can be verified from the outputs shown in Figures 4.5(f), 4.6(f) and 4.7(f).

Though from Tables 4.1 and 4.2 one can only see a slight difference between AWFcs and AWFa in their PSNR performance, AWFa can actually provide a subjectively better processing result than AWFa as a more flexible model is used in AWFa to handle more different scenarios in super resolution. Figure 4.8 serves as an example to show such a case. This justifies the usefulness of the anisotropic intensity covariance model proposed in this chapter.

The algorithms were also evaluated with the real LR images shown in Appendix C to investigate their performance in real situation. Figure 4.9 shows the reconstruction results of the 5th image. Similar observations can be found.

In AWFa, the directional covariance model is derived based on model function (3.4). In fact, the directional model can also be derived based on model function (3.1). We also derived such models and replaced the models used in AWFa with them to realize super-resolution image reconstruction. This version of AWFa is referred to as AWFa* and its PSNR performance is also included in Tables 4.1 and 4.2 for comparison. One can see that AWFa* is inferior to AWFa. It shows that a model in the form of function (3.1) is inferior to a model in the form of function (3.4) in this scenario as well.

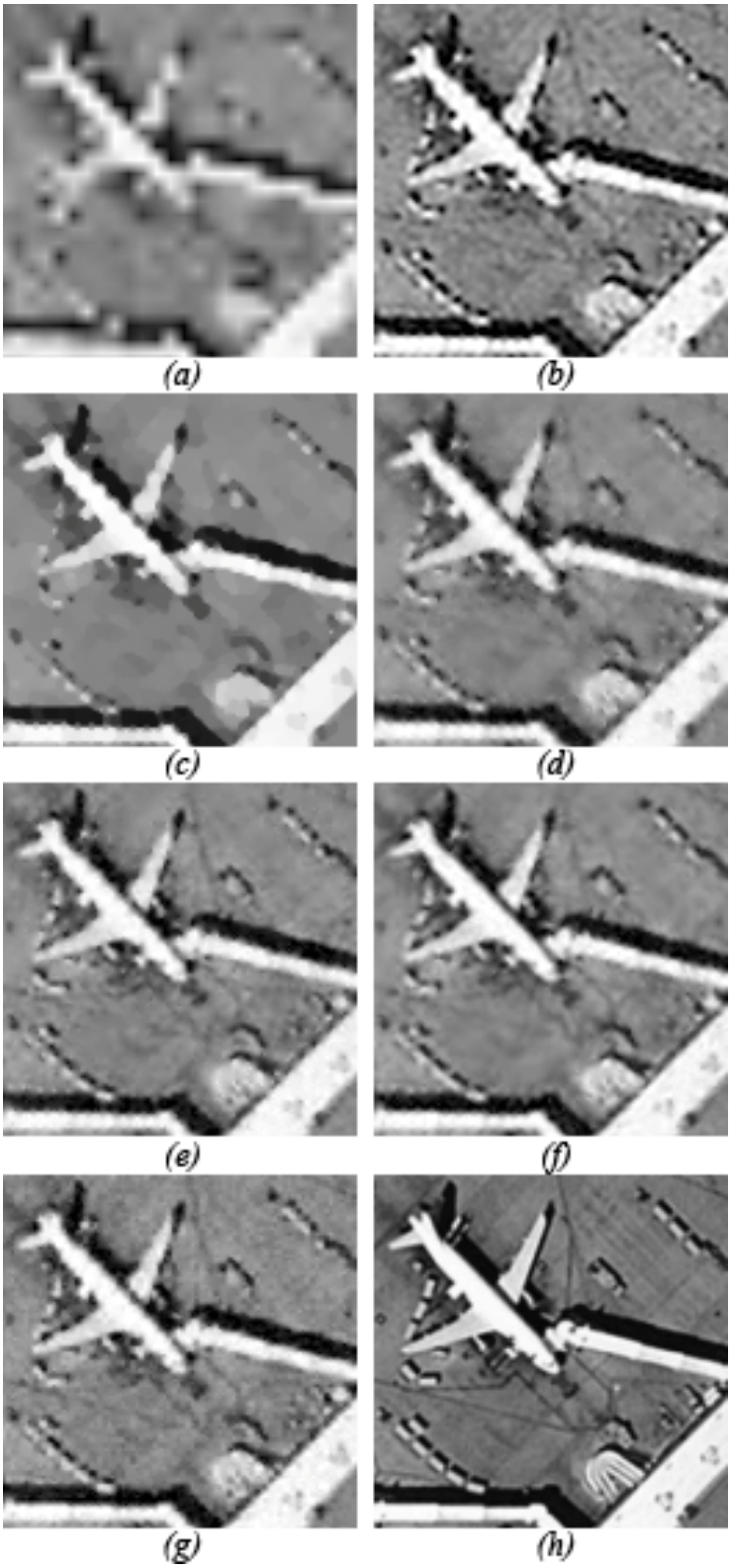

Figure 4.5 Parts of the super-resolution image reconstruction results of Image 8: (a) Bicubic, (b) Elad97, (c) Farsiu04, (d) AWFc, (e) AWFcs, (f) AWFa (g) Pham 06 and (h) the original

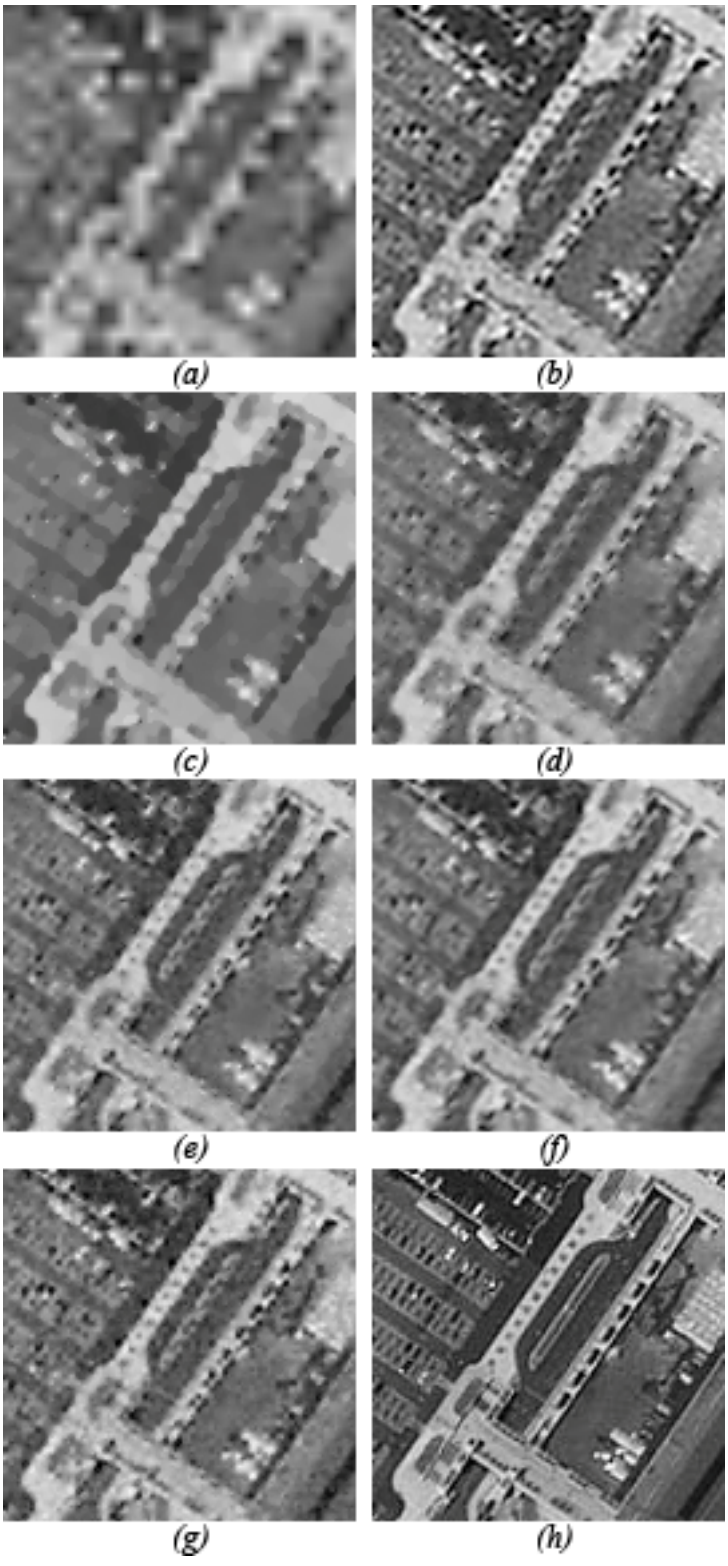

Figure 4.6 Parts of the super-resolution image reconstruction results of Image 4: (a) Bicubic, (b) Elad97, (c) Farsiu04, (d) AWFc, (e) AWFcs, (f) AWFa (g) Pham 06 and (h) the original

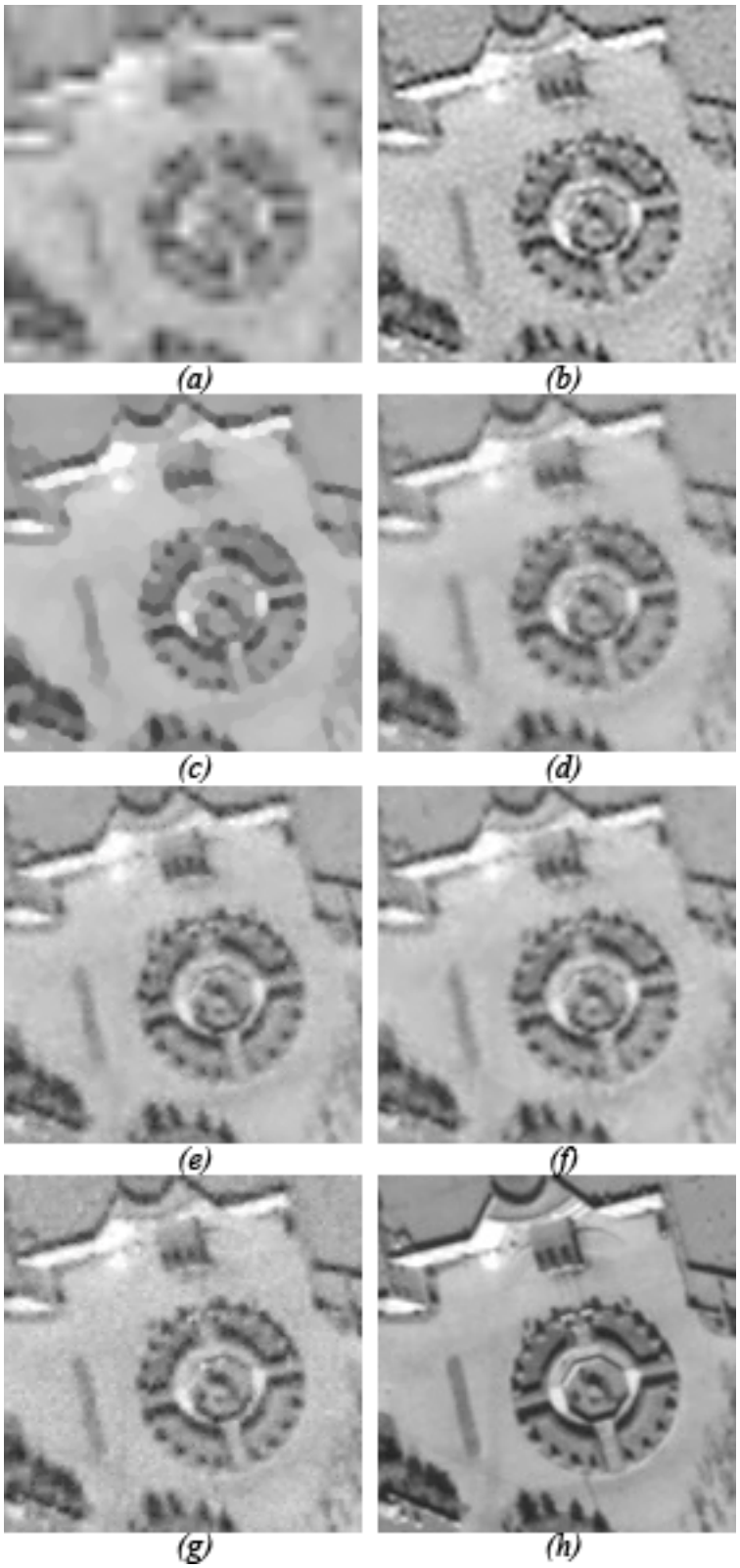

Figure 4.7 Parts of the super-resolution image reconstruction results of Image 3: (a) Bicubic, (b) Elad97, (c) Farsiu04, (d) AWFc, (e) AWFcs, (f) AWFa (g) Pham 06 and (h) the original

Figure 4.8 Enlarged super-resolution image reconstruction results of Image 8 for illustrating the effectiveness of AWFa. (a) AWFcs (b) AWFa (c) Original, with $\sigma_n^2 = 50$

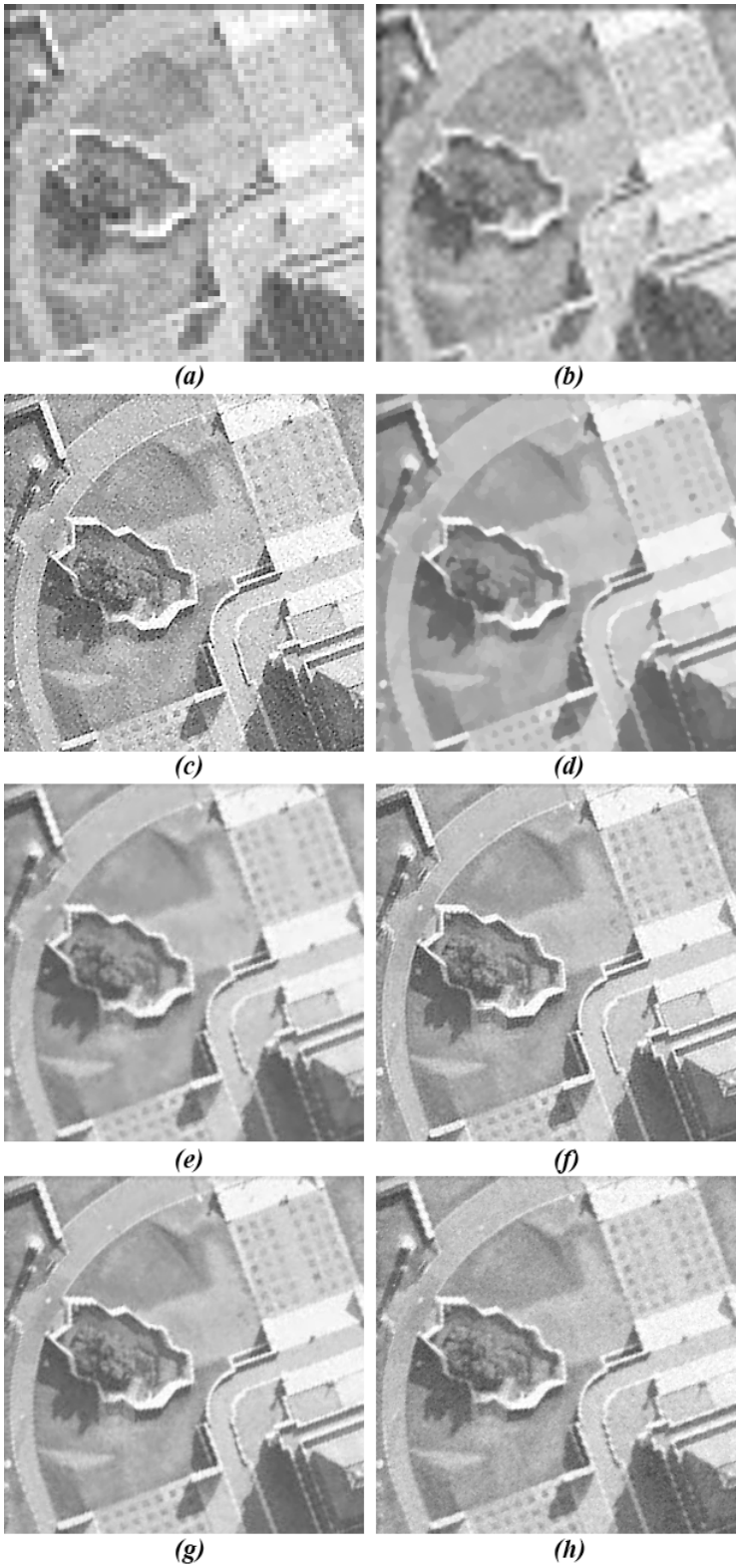

Figure 4.9 Parts of the super-resolution image reconstruction results obtained with real captured images: (a) interpolation by duplication, (b)Bicubic, (c) Elad97, (d) Farsiu04, (e) AWFc, (f) AWFcs, (g) AWFa and (h) Pham 06

4.4 Summary

In this chapter, a directional covariance model is proposed to model the local intensity covariance of a HR image based on the available LR pixels in the region. Specifically, we evaluate the sample variances of the LR pixels along various directions in the region and, based on the evaluation result, adjust the shape of covariance model function. Accordingly, the resultant anisotropic model can handle regions of directional features properly, which is impossible for conventional isotropic covariance models. With this directional intensity covariance model, an adaptive Wiener filtering algorithm can effectively improve the super-resolution image reconstruction performance as the algorithm can now adapt the estimation of HR pixels to both the local sample variance and the local edge characteristics. Simulation results show that the modification improves the super-resolution image reconstruction performance both objectively and subjectively.

The proposed directional covariance model relies on the detection of the edge orientation in a local region. For regions which have complicated textures or edges of different orientations, the model may not be able to handle it well. In that case, the model becomes isotropic to play safe. Another potential problem of the model is that the edge detection has to be based on the LR pixels as the HR image is unknown in practice. A wrongly detected the edge direction misguides the interpolation and hence introduces unexpected artifacts. These factors limit the performance of AWFa in the end. In the following chapter, this issue is addressed and an even better covariance model is proposed to tackle these potential problems.

Chapter 5

ADAPTIVE WIENER FILTERING WITH INTENSITY COVARIANCE MODELS RECTIFIED WITH LOW RESOLUTION SAMPLES

5.1 Introduction

Though a visible improvement in the super-resolution image reconstruction performance can be achieved with the directional covariance models introduced in Chapter 4, there is still room for further improvement. To a certain extent, AWFa tries to detect the edges and then rectify the covariance model according to the detected edge direction. This is not always easy to achieve. For example, it is not easy to detect a complicated edge especially when it is in a texture or noisy region. Besides, since the high resolution image is not available, the detection has to be based on the available low resolution images and hence the detection may not be accurate. To solve this problem, in this chapter we add an additional element to the intensity covariance model to take care of the edge characteristics implicitly such that no explicit edge detection is required.

In general, the more two pixel's intensity values are different, the more likely that the two pixels are separated by an edge or corrupted by noise. Based on this

observation, a new covariance model is defined to be a function of both the intensity difference and the geometric distance of two pixels. Without any explicit edge detection, the model automatically deemphasizes the correlation between two pixels which are not in the same side of an edge. Accordingly, the weights of the pixels for estimating the high resolution pixels can be determined more reliably with the covariance model, and a better super-resolution image reconstruction result can be obtained at the end.

This chapter is organized as follows. In Section 5.2, two covariance models are separately proposed. Both models use the intensity difference of the available LR samples in a local region to rectify an isotropic geometric-distance-based covariance model, which makes them automatically adapt to sophisticated local textures. Based on these two new models, a better adaptive Wiener filtering algorithm is then proposed. Some simulation results are reported in Section 5.3 to show the performance of the newly proposed adaptive Wiener filtering algorithm as compared with the conventional super-resolution image reconstruction algorithms. In the final section of this chapter, a brief summary is provided.

5.2 Rectified covariance model

In adaptive Wiener filtering, a HR pixel is estimated as a weighted sum of the registered LR pixels in its local region. The local intensity covariance of HR pixels, $r_{xx}(\Delta i, \Delta j)$, plays a significant role to determine the value of the weight. No matter AWFc[Hardie07], AWFsc or AWFa is used, $r_{xx}(\Delta i, \Delta j)$ is modeled as a function of the geometric distance between two HR pixels as given in eqn. (3.1), (3.4) or (4.4).

In general, two pixels are more correlated when they are closer to each other. However, this stationary spatial covariance model simplifies the real situation as it does not take the regional edge characteristics into account. Obviously, an edge breaks the correlation between the pixels in different sides of the edge and hence the

covariance model should be directional and non-stationary.

A remedial solution is to detect the edges and then rectify the covariance model according to the detected edge direction as shown in Chapter 4. However, this approach does not always work properly. First, it is not easy to detect an edge when there is noise. Second, the HR image is not available and hence the detection has to be based on the available LR images. It is difficult to locate an edge accurately in the HR image to be estimated as a lot of HR samples are missing at the moment. Third, available edge detection schemes may not be able to handle complicated curves well especially in a texture region.

To solve this problem, in our proposed solution we add an additional element to the covariance model to take care of the edge characteristics implicitly such that no explicit edge detection is required.

In general, the intensity values of the samples in the same side of an edge are more or less the same while those in different sides are very different. The more two pixel's intensity values are different, the more likely that the two pixels are separated by an edge or corrupted by noise. In other words, they are likely to be more uncorrelated.

Based on this idea, two new covariance models are proposed in this chapter. One describes the covariance between two x samples located at positions of the observed LR pixels. These positions are marked with crosses in the example shown in Figure 2.4. The other one describes the covariance between a x sample located at the position of an observed LR pixel and a x sample located at the position of a HR pixel to be estimated. The position of the former x sample is marked with a red cross in the example shown in Figure 2.4 while that of the latter x sample is marked with a blue circle.

The former covariance models are used to estimate auto-covariance matrix R while the latter is used to estimate cross-covariance matrix P. As discussed in Section 2.5, these two matrices play a critical role in determining the weights of the available

LR pixels when estimating the HR pixels in the same local region. For reference, these two new covariance models are, respectively, referred to as homogeneous model and heterogeneous model hereafter. Besides, as in Section 2.4, the set of the locations of the observed LR pixels and the set of the locations of the HR pixels to be estimated are, respectively, referred to as Ω_l and Ω_h.

Homogeneous model:

Let (i,j) and $(i+\Delta i,j+\Delta j)$ be the positions of any two x samples of interest in this model. As both (i,j) and $(i+\Delta i,j+\Delta j)$ belong to Ω_l, $y(i,j)$ and $y(i+\Delta i,j+\Delta j)$ are known because of prior registration. The covariance model for this situation is proposed as follows.

$$\begin{aligned} r_{xx}(\Delta i,\Delta j) &= \sigma_x^2\left(e^{-\frac{\Delta i^2+\Delta j^2}{\gamma}}\right)\left(e^{-\frac{|y(i,j)-y(i+\Delta i,j+\Delta j)|}{\sqrt{2}\sigma_n}}\right) \\ &= \sigma_x^2\left(e^{-\left(\frac{\Delta i^2+\Delta j^2}{\gamma}+\frac{|y(i,j)-y(i+\Delta i,j+\Delta j)|}{\sqrt{2}\sigma_n}\right)}\right) \end{aligned} \tag{5.1}$$

where σ_x^2 is the local variance of the HR image and σ_n^2 is the noise variance.

There are two components, namely,

$$r_{g.d.}(\Delta i,\Delta j) = \exp(-(\Delta i^2+\Delta j^2)/\gamma) \tag{5.2}$$

and

$$r_{i.d.}(\Delta i,\Delta j) = \exp(-|y(i,j)-y(i+\Delta i,j+\Delta j)|/\sqrt{2}\sigma_n) \tag{5.3}$$

in this proposed model function. The first one takes the geometric distance between two pixels into account while the second one takes the observed intensity difference

of the two pixels into account. This covariance model reflects the fact that two pixels are highly uncorrelated when the intensity values of their noisy blurred versions are very different even though they are close in geometric distance. By considering that $y(i,j) = f(i,j)+n(i,j)$ and $f(i+\Delta i,j+\Delta j)) \approx f(i,j) = x(i,j)*b(i,j)$ in a smooth local region, we have $E\{(y(i,j)- y(i+\Delta i,j+\Delta j))^2\} \approx E\{(n(i,j)-n(i+\Delta i,j+\Delta j))^2\} = 2\sigma_n^2$. Hence, $|(y(i,j)-y(i+\Delta i,j+\Delta j))|$ is scaled with $1/\sqrt{2}\sigma_n$ to tolerate the noise in $r_{i.d.}(\Delta i,\Delta j)$. σ_n is assumed to be known.

Parameters γ is used to control the effect of the two components and weight their contribution to the model. They can be determined with some training video sequences via an empirical study. In our study, γ is selected to be 5.

Figure 5.1 shows how $r_{g.d.}(\Delta i,\Delta j)$ and $r_{i.d.}(\Delta i,\Delta j)$ contribute to the intensity correlation between two HR pixels in regions of different natures. In particular, Figure 5.1 (a) shows four noisy blurred regions which contain complicated edges, smooth intensity transition, texture and a straight edge respectively. By using Figure 5.1 (a) as the observed LR images, the intensity correlation between any pixel in a particular region and the center pixel of the region is derived with eqn. (5.1), and its normalized contour plot is plotted in Figure 5.1 (d). The proposed model adapts to the local characteristics of a region. Without any explicit edge detection, it automatically rejects or deemphasizes the pixels which are not in the same side of an edge with the pixel of interest. Accordingly, the weights of the pixels for estimating the HR pixels can be determined more reliably with the covariance model, and a better super-resolution image reconstruction result can be obtained at the end.

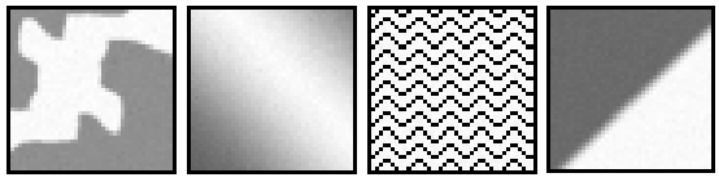

(a)

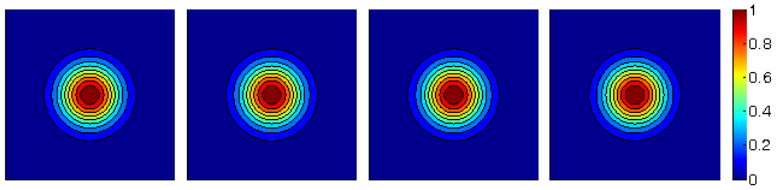

(b)

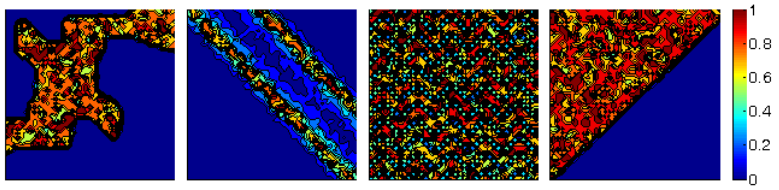

(c)

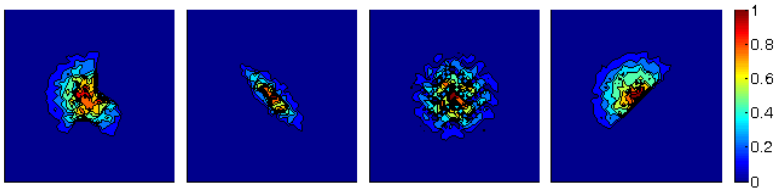

(d)

Figure 5.1 Normalized covariance models for regions of various nature: (a) Observed noisy LR images (SNR=40dB); (b) contribution of $r_{g.d.}(\Delta i, \Delta j)$ to the proposed model; (c) contribution of $r_{i.d.}(\Delta i, \Delta j)$ to the proposed model; and (d) proposed model

Heterogeneous model:

This covariance model describes the covariance between a x sample located at the position of an observed LR pixel and a x sample located at the position of a HR pixel to be estimated. Let $(i+\Delta i, j+\Delta j) \in \Omega_l$ and $(i,j) \in \Omega_h$ be, respectively, the positions of these two x samples of interest. In such a case, $y(i+\Delta i, j+\Delta j)$ is known. However, as neither $y(i,j)$ nor $x(i,j)$ is known, estimation has to be carried out and the covariance model is modified from the one suggested in eqn. (5.1) as

$$r_{xx}(\Delta i,\Delta j)=\sigma_x^2\left(e^{-\frac{\Delta i^2+\Delta j^2}{\gamma}}\right)\left(e^{-\frac{\left|\hat{f}(i,j)-y(i+\Delta i,j+\Delta j)\right|}{\sigma_n}}\right) \tag{5.4}$$

where $\hat{f}(i,j)$ is an estimate of $f(i,j)=x(i,j)*b(i,j)$. In a smooth local region, we should have $f(i+\Delta i,j+\Delta j)) \approx f(i,j) \approx \hat{f}(i,j)$ when Δi and Δj are small. Accordingly, we have $E\{(\hat{f}(i,j) - y(i+\Delta i,j+\Delta j))^2\} \approx E\{(n(i+\Delta i,j+\Delta j))^2\} = \sigma_n^2$ and hence $|\hat{f}(i,j) - y(i+\Delta i, j+\Delta j)|$ is scaled with $1/\sigma_n$ to tolerate the noise when it is used to rectify the covariance model.

In either covariance model shown in eqn (5.1) or (5.4), σ_x^2 is the local variance of the unknown HR pixels and it has to be estimated with the LR pixels in the local region. In our realization, σ_x^2 is estimated as

$$\sigma_x^2=\max\left\{(\sigma_y^2-\sigma_n^2)/C_o,0\right\} \tag{5.5}$$

where σ_y^2 is the variance of all LR pixels registered in the region, σ_n^2 is the noise variance and

$$C_o=\int_{i=-\infty}^{\infty}\int_{j=-\infty}^{\infty}e^{-(i^2+j^2)/\gamma}\cdot(b(i,j)*b(-i,-j))\cdot di\cdot dj \tag{5.6}$$

where $b(i,j)$ is the blurring function discussed in Section 2.5. By following the steps detailed in Section 2.5, the weights of all LR pixels used to estimate a HR pixel in the region can be determined and, accordingly, the HR image can be obtained by adaptive Wiener filtering.

Estimation of $\hat{f}(i,j)$:

As mentioned earlier, estimates of $\hat{f}(i,j)$ for $(i,j)\in\Omega_h$ are required to derive the covariance model defined in eqn. (5.4). As we have $f(i,j) = x(i,j)*b(i,j)$ and $b(i,j)$ is known, $\hat{f}(i,j)$ can be determined as long as $x(i,j)$ is known. Hence, a preliminary estimate of $x(i,j)$ is required.

Various approaches such as a bilinear interpolation of the available LR pixels can be used to estimate $x(i,j)$. In our approach, we replace covariance models shown in eqns. (5.1) and (5.4) with

$$r_{xx}(\Delta i,\Delta j) = \sigma_x^2 \exp(-(\Delta i^2 + \Delta j^2)/\gamma) \tag{5.7}$$

and then use the same proposed algorithm with covariance model shown in eqn. (5.7) to get the preliminary estimate of $x(i,j)$.

Figure 5.2 summaries the overall workflow of the proposed super-resolution image reconstruction algorithm.

The modification presented in this chapter to AWFc results in another new adaptive Wiener filtering algorithm. This algorithm derives the correlation between two pixels in a local region based on (i) their geometric distance and (ii) the known or estimated intensity difference between their LR samples. Based on the derivation results, it adaptively adjusts the weights of the involved LR pixels when estimating the HR pixels in a region. As the derivation of the intensity covariance model exploited in the algorithm can be viewed as a process of rectifying a conventional geometric-distance-based intensity covariance model with the intensity difference of the available local LR pixels , this algorithm is referred to as AWFr for reference hereafter.

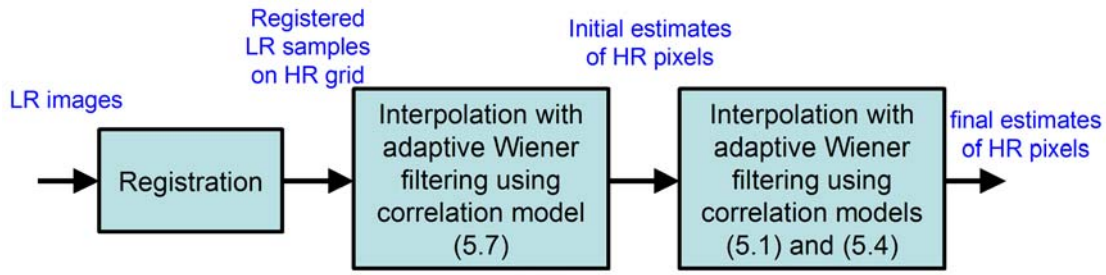

Figure 5.2 Flow of the proposed super-resolution image reconstruction algorithm

5.3 Simulation results

Simulations were carried out to evaluate the performance of the proposed algorithm. The set of twenty 8-bit gray level aerial images shown in Appendix A were used as original HR images in the simulation. All of them are of original size 500×500 pixels. For each one of them, a sequence of 10 LR images was generated as follows.

First of all, a sequence of real value displacement vectors was randomly generated in a way that the value of each of their elements was bounded by ±2. The HR image was then translationally shifted by sub-pixel spacing using bicubic interpolation, blurred with a Gaussian filter of size 5×5, down-sampled by 5 in both horizontal and vertical directions, and finally corrupted with additive zero-mean random noise of variance σ_n^2. The translational shift for the k^{th} image in the sequence was set to be the accumulated sum of the first k-1 aforementioned displacement vectors.

The original HR images were estimated with their corresponding LR sequences in the simulation. The ratio of the target resolution of the reconstructed HR image to the resolution of a LR image for each dimension is 5. A sliding window of size 15×15 pixels moves over the HR grid to reconstruct the 5×5 HR pixels in the center region of the window. The initial sub-pixel registration step was carried out with the algorithm proposed in [Keren88].

Tables 5.1 and 5.2 show the performance achieved with different super-resolution image reconstruction algorithms in terms of *PSNR* under noise conditions σ_n^2=25 and σ_n^2=50. One can see that the average performance of AWFr is better than other conventional SR algorithms in terms of PSNR. Another interesting observation is that AWFr's PSNR improvement with respect to AWFc[Hardie07] is remarkably larger than AWFa's and AWFcs's.

Table 5.3 shows the performance of various algorithms under noise condition σ_n^2=100. One can see that AWFr is not sensitive to the noise as AWFcs, AWFa and AWFc. It is still able to provide better results than the others.

In AWFa, the intensity values of local LR pixels are used to rectify a geometric-distance-based model which is in a form of function (5.2). Actually one can also apply the same idea presented in this chapter to rectify a geometric-distance-based model in the form of function (3.1). This version of AWFr is referred to as AWFr* and its performance is also shown in Tables 5.1 and 5.2 for comparison. One can see that AWFr* is inferior to AWFr. This shows that a geometric-distance-based covariance model in the form of function (3.1) does not work properly with the idea presented in this chapter.

Figures 5.3-5.5 show parts of the simulation results of different super-resolution image reconstruction algorithms for visual comparison. The input LR sequences are corrupted with random Gaussian noise of σ_n^2=25 and σ_n^2=50. In general, the proposed algorithm provides sharper and more robust interpolation results than the other evaluated algorithms. By rectifying a conventional geometric-distance-based intensity covariance model with the intensity difference of the available local LR pixels, the proposed algorithm takes good care of the noise and the local edge characteristics implicitly and provides a good super-resolution image reconstruction result.

Noise		σ_n^2=25								
Image		Bicubic	Elad97	Farsi04	AWFc	Pham06	AWFcs	AWFa	AWFr	AWFr*
PSNR (dB)	1	19.00	20.49	21.30	25.42	25.42	26.02	26.06	26.17	25.42
	2	18.66	20.15	20.93	24.80	24.77	25.35	25.44	25.28	24.77
	3	21.01	23.32	23.99	29.24	29.25	29.74	29.89	30.48	29.25
	4	17.62	19.35	18.24	22.49	22.50	22.98	23.08	23.21	22.47
	5	18.93	20.92	21.21	25.08	25.07	25.44	25.51	25.26	25.07
	6	22.42	22.79	23.98	27.64	27.72	27.47	28.18	27.42	27.65
	7	17.86	18.81	19.88	22.34	22.35	22.51	22.37	22.47	22.35
	8	17.95	19.95	20.66	25.28	25.29	25.99	26.27	27.35	25.27
	9	17.28	18.83	19.53	23.63	23.64	24.56	24.58	24.97	23.62
	10	17.71	18.97	19.87	24.17	24.12	24.53	24.57	24.64	24.17
	11	16.6.0	17.92	18.72	22.76	22.75	22.93	23.25	23.24	22.75
	12	18.22	20.41	21.02	26.17	26.16	27.03	27.25	29.05	26.17
	13	18.17	20.47	21.13	26.65	26.66	27.54	27.76	29.00	26.67
	14	19.34	20.95	21.83	25.94	25.95	26.63	26.94	27.70	25.94
	15	18.65	20.11	20.89	24.89	24.89	25.08	25.36	25.21	24.86
	16	17.90	19.70	20.32	23.84	23.85	24.52	24.53	24.22	23.83
	17	18.48	19.71	20.54	23.80	23.79	24.16	24.04	23.48	23.81
	18	20.11	21.81	22.61	26.32	26.31	26.42	27.06	26.52	26.31
	19	17.82	19.16	20.00	23.41	23.43	23.86	23.88	23.35	23.39
	20	17.29	18.75	19.47	23.25	23.23	23.11	23.66	23.36	23.21
	Average:	18.55	20.13	20.81	24.86	24.86	25.29	25.48	25.62	24.85
Average Time:		0.02s	15.74s	45.16s	25.15s	29.21s	25.54s	39.78s	35.75s	26.82s

Table 5.1 *PSNR* performance (in dB) and computation time of various super-resolution image reconstruction algorithms under noise condition $\sigma_n^2 = 25.$

Noise		σ_n^2=50								
Image		Bicubic	Elad97	Farsiu04	AWFc	Pham06	AWFcs	AWFa	AWFr	AWFr*
PSNR (dB)	1	18.94	20.33	21.29	25.11	25.12	25.67	25.66	25.75	25.10
	2	18.61	20.00	20.91	24.59	24.57	25.07	25.12	25.07	24.50
	3	20.92	23.03	23.92	28.71	28.19	28.96	29.08	29.64	28.69
	4	17.58	18.16	19.38	22.25	22.28	22.75	22.83	22.84	22.34
	5	18.86	20.34	21.21	24.86	24.81	25.16	25.17	25.00	24.82
	6	22.27	22.55	23.96	27.52	27.08	27.10	27.37	27.57	27.50
	7	17.80	18.73	19.88	22.21	22.18	22.02	22.18	22.03	22.17
	8	17.90	19.82	20.64	25.05	25.02	25.66	25.92	26.68	25.06
	9	17.24	18.85	19.65	23.13	23.42	24.31	24.27	24.86	23.39
	10	17.66	18.86	19.86	23.91	23.93	24.27	24.26	24.35	23.90
	11	16.57	17.84	18.71	22.54	22.57	23.02	23.02	23.07	22.59
	12	18.18	20.30	21.02	25.78	25.85	26.64	26.80	28.13	25.85
	13	18.10	20.32	21.12	26.10	26.32	27.01	27.16	28.24	26.33
	14	19.29	20.80	21.79	25.69	25.66	25.87	26.53	27.08	25.71
	15	18.58	20.30	21.08	24.74	24.69	24.89	25.02	24.94	24.70
	16	17.84	19.59	20.00	23.64	23.69	24.26	24.24	23.85	23.67
	17	18.42	19.59	20.54	23.58	23.58	23.13	23.78	23.39	23.58
	18	20.04	21.62	22.60	26.05	26.12	26.69	26.68	26.28	26.12
	19	17.78	19.06	20.00	23.24	23.20	22.91	23.31	23.20	23.18
	20	17.26	18.65	19.48	23.04	23.05	22.46	23.42	23.28	23.02
	Average:	18.49	19.94	20.85	24.59	24.57	24.89	25.09	25.26	24.61
Average Time:		0.02s	15.74s	45.16s	25.15s	29.21s	25.54s	39.78s	35.75s	26.82s

Table 5.2 *PSNR* performance (in dB) and computation time of various super-resolution image reconstruction algorithms under noise condition $\sigma_n^2 = 50$.

Noise		σ_n^2=100								
Image		Bicubic	Elad97	Farsiu04	AWFc	Pham06	AWFcs	AWFa	AWFr	AWFr*
PSNR (dB)	1	18.82	20.05	21.26	23.99	23.93	24.97	24.97	25.10	24.67
	2	18.46	19.76	20.89	24.23	24.20	24.30	24.53	24.66	24.23
	3	20.73	22.53	23.84	27.14	27.18	27.80	28.15	28.45	27.97
	4	17.49	17.98	19.34	21.93	22.02	22.34	22.22	22.41	21.95
	5	18.75	20.03	21.17	24.41	24.40	23.95	23.85	24.58	24.41
	6	22.00	22.23	24.10	26.84	26.99	26.43	25.64	27.47	27.09
	7	17.73	18.50	19.84	21.91	21.94	21.96	21.72	21.61	21.95
	8	17.81	19.57	20.62	24.30	24.67	25.00	25.21	25.96	24.59
	9	17.16	18.69	19.67	23.08	23.03	22.77	23.15	24.37	23.15
	10	17.58	18.67	19.85	23.56	23.17	23.18	23.32	23.86	23.56
	11	16.51	17.71	18.72	22.26	22.19	21.81	21.56	22.68	22.25
	12	18.09	20.07	21.00	25.30	25.30	22.98	22.92	27.11	25.36
	13	17.99	20.02	21.10	25.17	25.10	26.19	26.29	27.05	25.74
	14	19.15	20.52	21.78	25.25	25.23	23.82	23.86	26.15	25.25
	15	18.48	20.02	21.06	24.37	24.36	24.43	24.28	24.59	24.35
	16	17.75	19.35	20.30	23.37	23.42	23.19	23.32	23.64	23.38
	17	18.33	19.37	20.54	23.28	23.27	23.17	22.88	23.20	23.30
	18	19.89	21.28	22.58	25.78	25.77	25.29	25.27	25.95	25.82
	19	17.68	19.62	19.66	22.21	22.29	22.97	22.86	22.91	22.87
	20	17.20	18.50	19.47	22.17	22.10	22.13	21.72	22.87	22.79
	Average:	18.38	19.72	20.84	24.03	24.03	23.93	23.89	24.73	24.23
Average Time:		0.02s	15.74s	45.16s	25.15s	29.21s	25.54s	39.78s	35.75s	26.82s

Table 5.3 *PSNR* performance (in dB) and computation of various super-resolution image reconstruction algorithms under noise condition $\sigma_n^2 = 100$.

Figure 5.3 Parts of the super-resolution image reconstruction results of Image 3: (a) Bicubic, (b) Elad97, (c) Farsiu04, (d) AWFcs, (e) AWFa, (f) AWFr, (g) AWFc, (h) Pham06 and (i) the original

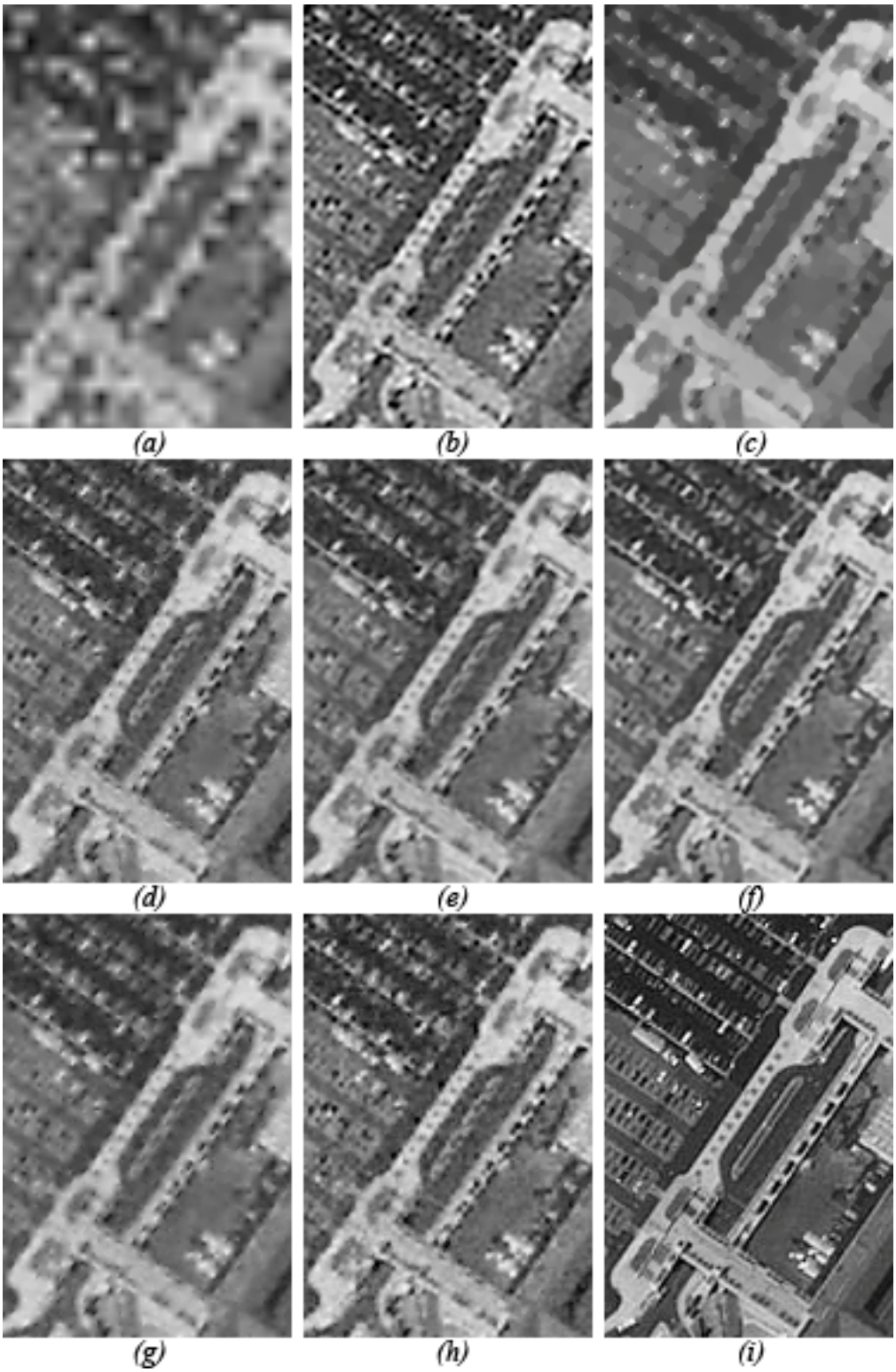

Figure 5.4 Parts of the super-resolution image reconstruction results of Image 4: (a) Bicubic, (b) Elad97, (c) Farsiu04, (d) AWFcs, (e) AWFa, (f) AWFr, (g) AWFc, (h) Pham06 and (i) the original

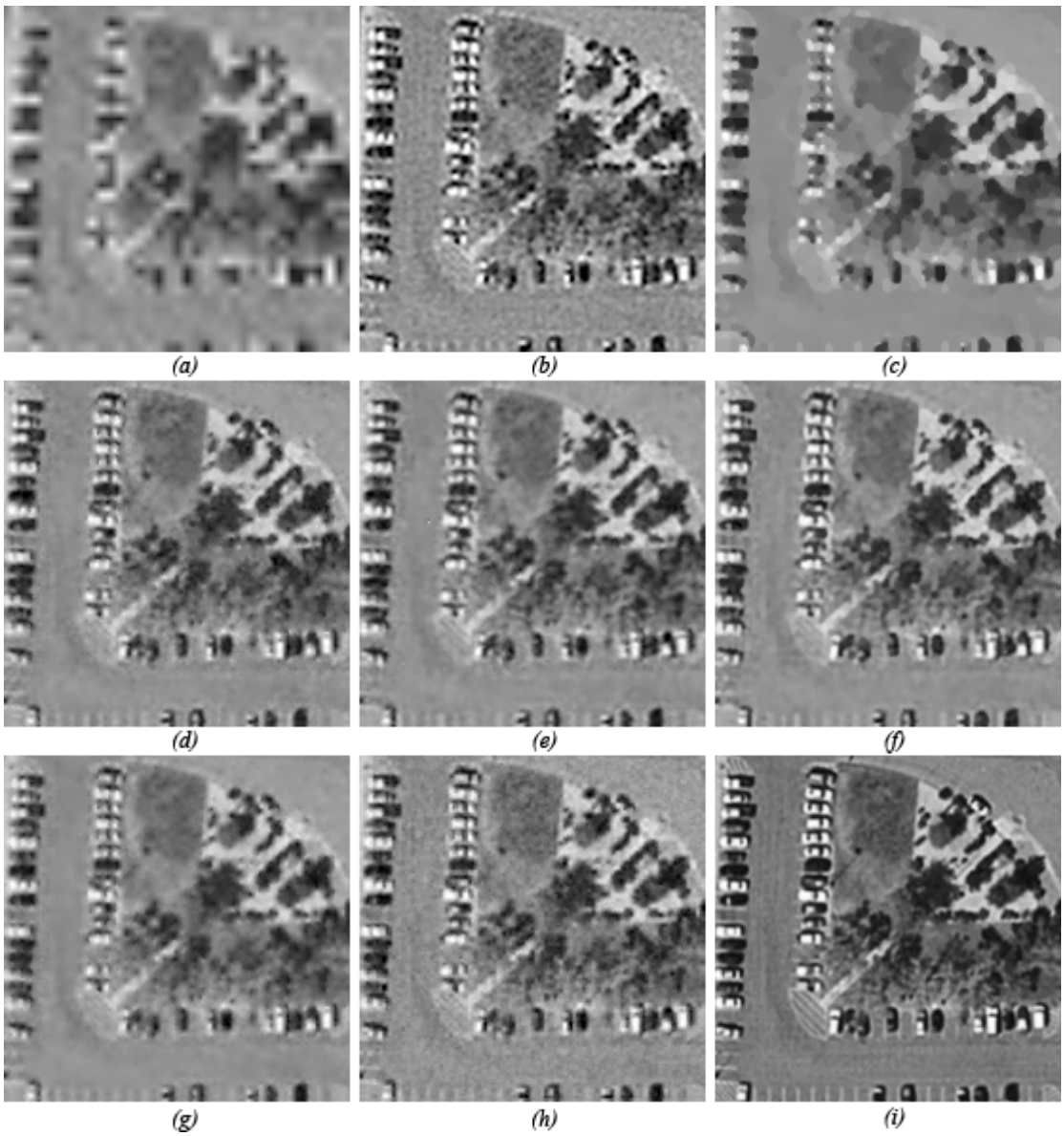

Figure 5.5 Parts of the super-resolution image reconstruction results of Image 12: (a) Bicubic, (b) Elad97, (c) Farsiu04, (d) AWFcs, (e) AWFa, (f) AWFr, (g) AWFc, (h) Pham06 and (i) the original

(a) (b) (c)

Figure 5.6 Super-resolution image reconstruction results obtained with different adaptive Wiener filtering algorithms: (a) AWFa (b) AWFr and (c) Original.

For a better visual comparison of the outputs of AWFa and AWFr, Figure 5.6 shows the enlarged results of the outputs of AWFa and AWFr. The input LR sequences are corrupted with random Gaussian noise of σ_n^2=50. One can see that AWFr does not only produce finer edges and sharper texture, but remove more noise as well.

The algorithms were also evaluated with the real LR images shown in Appendix C to investigate their performance in real situation. Figure 5.7 shows the reconstruction results of the 5th image. Similar observations can be found.

In the proposed algorithm, a preliminary estimate of $\hat{f}(i,j)$ for $(i,j)\in\Omega_h$ are required to derive the covariance model defined in eqn. (5.4) and its estimation is suggested in Section 5.2. A study was carried out to see if some other conventional approaches could also provide a good preliminary estimate for deriving the covariance model. The testing data was generated in the same way as presented earlier. Table 5.3 shows the performance of various approaches for comparison and it can be found that the suggested solution is an appropriate solution to achieve the goal.

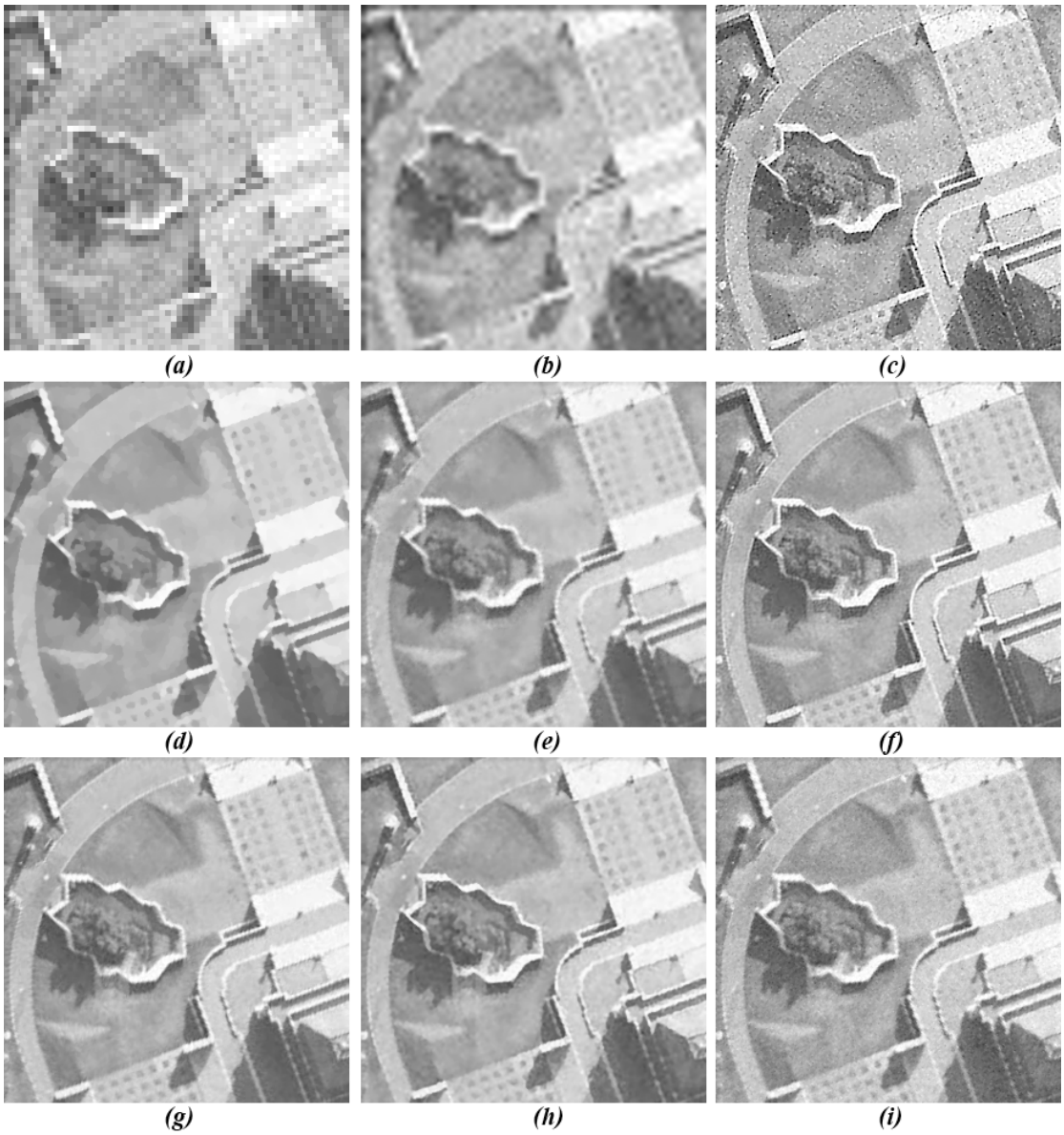

Figure 5.7 Parts of the super-resolution image reconstruction results obtained with real captured images: (a) interpolation by duplication, (b)Bicubic, (c) Elad97, (d) Farsiu04, (e) AWFc, (f) AWFcs, (g) AWFa, (h)AWFr, and (i) Pham06

Method for obtaining preliminary estimates	Noise condition		
	σ_n^2=25	σ_n^2=50	σ_n^2=100
Bilinear	17.19	18.57	18.70
Hardie07	25.11	24.85	24.46
the proposed	25.62	25.26	24.73

Table 5.4 Average *PSNR* performance (in dB) achieved by AWFr with different preliminary estimates of HR pixels obtained with different approaches

5.4 Summary

Two intensity covariance models are proposed in this chapter. One is for describing the covariance between two HR pixels located at positions of observed LR pixels while the other one is for describing the covariance between two HR pixels one of which is located at positions of observed LR pixels. Each model is in a form of a function of the geometric distance of two pixels and the intensity difference of the known or estimated LR samples of the pixels.

In AWFc[Hardie07], AWFcs and AWFa, we have one model for each local region. The covariance of any pair of pixels in the same region is derived based on the same model. When the texture in the region is very complicated, one may not be able to use the shared covariance model to accurately estimate the covariance between a particular pair of pixels in the region. On the contrary, we have one dedicated model for each pair of pixels in AWFr. No compromise is required for the model to take care of all pixels in the region. Consequently, the proposed models can faithfully reflect the real covariance between two pixels in a region and fully adapt to the local characteristics of a region. Without any explicit edge detection, it automatically

rejects or deemphasizes the pixels which are not in the same side of an edge with the pixel of interest.

Based on the newly proposed covariance models, a better adaptive Wiener filtering algorithm (AWFr) for super-resolution image reconstruction is proposed. As the weights of the pixels for estimating the HR pixels can be determined more reliably with the covariance model, a better super-resolution image reconstruction result can be obtained with AWFr at the end. Simulation results show the effectiveness of this super-resolution image reconstruction algorithm in terms of both objective and subjective criteria.

Chapter 6

CONCLUSTIONS AND FUTURE WORK

6.1 Conclusions

This dissertation addresses the issue of enhancing the performance of adaptive Wiener filtering in super-resolution image reconstruction. In particular, three modifications to the conventional adaptive Wiener filtering algorithm [Hardie07] are proposed in this work. All of them are based on the utilization of a better intensity covariance model in the derivation of the Wiener filter coefficients.

In Hardie's adaptive Wiener filtering algorithm [Hardie07], the intensity covariance model of two samples in a local region is formulated as an isotropic function of (i) the geometric distance between two samples and (ii) the local variance of the observed low resolution pixels in the region. Though this simple model reflects the correlation of two pixels in the general situation to a certain extent, it is not appropriate to describe the pixel correlation in a local region with presence of edge or texture.

The first suggested modification to Hardie's adaptive Wiener filtering algorithm is based on the fact that pixels are more correlated in a non-edge region than an edge region in practice. This is because an edge breaks the correlation between the pixels in different sides of an edge. Accordingly, the covariance model for regions having an

edge should be different from the covariance model for regions without an edge. In this first modified adaptive Wiener filtering algorithm, local regions are classified into either edge regions or non-edge regions, and then corresponding covariance models are used to derive the weights for individual regions.

The idea is further extended in our second suggested modification to Hardie's adaptive filtering algorithm. Obviously, pixels along an edge should be more correlated than those pixels in different sides of the edge, and hence the covariance model function should be anisotropic according to the dominant edge orientation in a local region. In our second modification proposal, we evaluate the sample variances along various directions in a local region and, based on the evaluation result, adjust the shape of covariance model function. By doing so, the orientation of the covariance model function and the extent of its asymmetricity are fully adaptive to the dominant orientation of the texture in the region of interest. Unlike the approach adopted in our first proposed modification, no explicit region classification is required.

In all adaptive Wiener filtering algorithms so far discussed in this chapter, all pairs of pixels in the same region follow the same intensity covariance model. However, when one probes into the issue further, one can find that the intensity correlation between pixels in a region is actually different from pair to pair. In our final proposal, each pair of pixels in a local region has its spatial intensity covariance model rectified by their known observed or estimated low resolution samples. As a consequence, every single pair of pixels has its own covariance model which is in a form of a function of both (i) their geometric distance and (ii) the intensity difference of their low resolution samples. A local Wiener filter is then possible to fully adapt to the local context of a region. Unlike the approach suggested in our second modification to Hardie's algorithm, no explicit edge detection is required. This is critical when the low resolution images are too noisy for one to detect the edges.

Simulation results show that all three proposed modifications to Hardie's algorithm are able to improve the performance of adaptive Wiener filtering in

super-resolution image reconstruction in terms of both subjective and objective criteria, and the last one provides the best performance among them.

6.2 Future works

In this work, we put our focus on the reconstruction of super-resolution images based on raw low resolution images. In practice, we might only have compressed low resolution images available for the reconstruction. Sometimes these compressed images may even be encoded with different lossy codecs such that the quality of the low resolution images varies from image to image. A lossy compression introduces extra distortion to the observed images, and hence the observation model has to be revised.

In adaptive Wiener filtering, high resolution pixels in a local region are estimated as weighted sums of the low resolution samples in the same region. When the quality of the available compressed low resolution images is different, the contribution of the samples from different low resolution images to the estimation should also be weighted so as to take care of the situation. Accordingly, the cost function to be minimized when deriving the Wiener filter coefficients should be adjusted to take this factor into account.

In all interpolation-based super-resolution image reconstruction algorithms, a registration process is required for registering each observed low resolution sample onto a two-dimensional reference space such that a subsequent non-uniform interpolation can be done accordingly. It is not always easy to register low resolution images accurately especially when the observed images are noisy and when deformed objects appear in the observed images. Empirically, the various adaptive Wiener filtering algorithms presented in this thesis work with the registration algorithm proposed by [Irani91] to provide a good super-resolution image reconstruction performance in our simulation results. However, it would be interesting to devote some more effort to investigate the impact of the registration to the performance of

adaptive Wiener filtering.

In this work, our focus is on remote sensing applications. The data to be processed are aerial images in which there is only a global translation between images. This simplifies the situation a bit. For other applications such as high-definition television, there can be a number of objects in the scene and their motion is not limited to translation. The registration problem can become very complicated. It would be a meaningful direction for one to modify the proposed adaptive Wiener filtering algorithms to handle such a problem and hence support other applications.

Appendix A

TESTING IMAGES

Image.1

Image.2

Image.3

Image.4

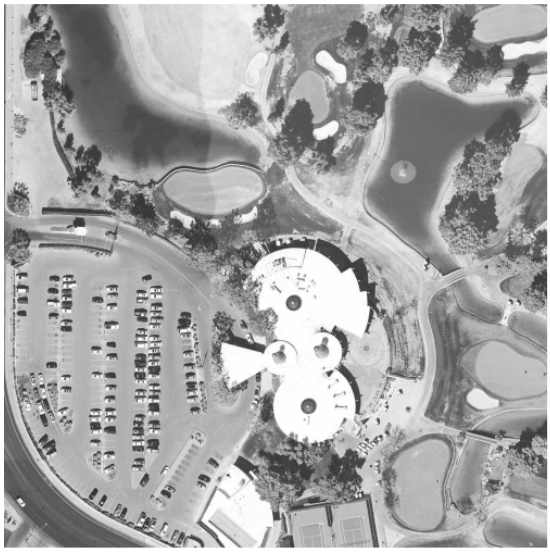

Image.5

Image.6

Image.7

Image.8

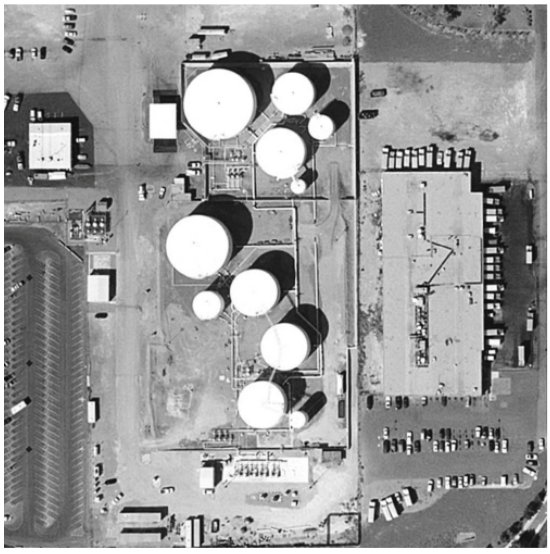

Image.9

Image.10

Image.11

Image.12

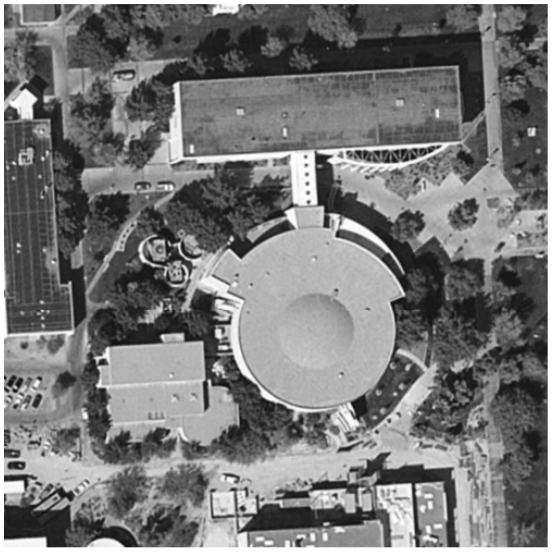

Image.13

Image.14

Image.15

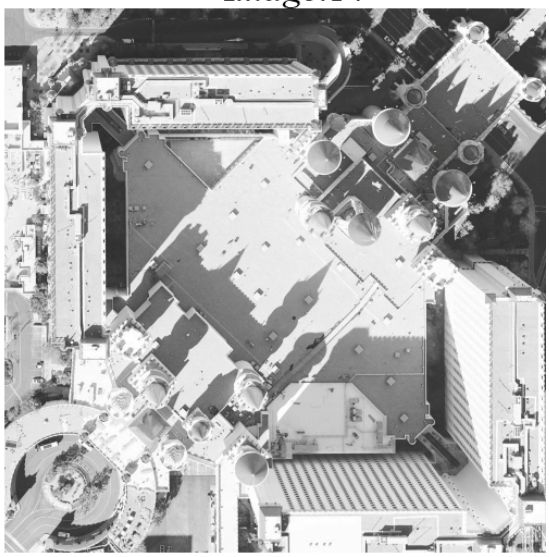

Image.16

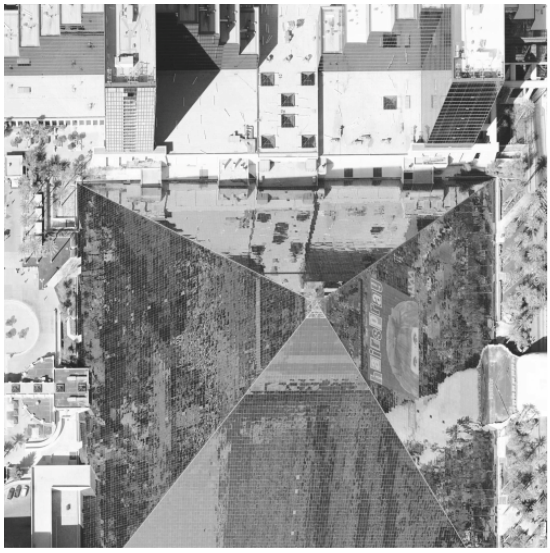

Image.17

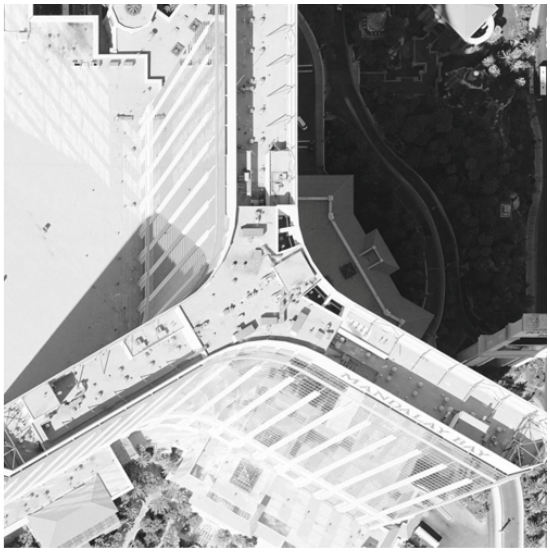

Image.18

Image.19

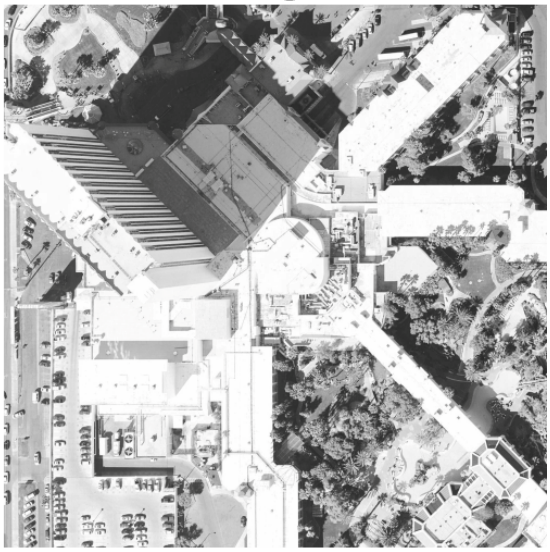

Image.20

Appendix B

TRAINING IMAGES

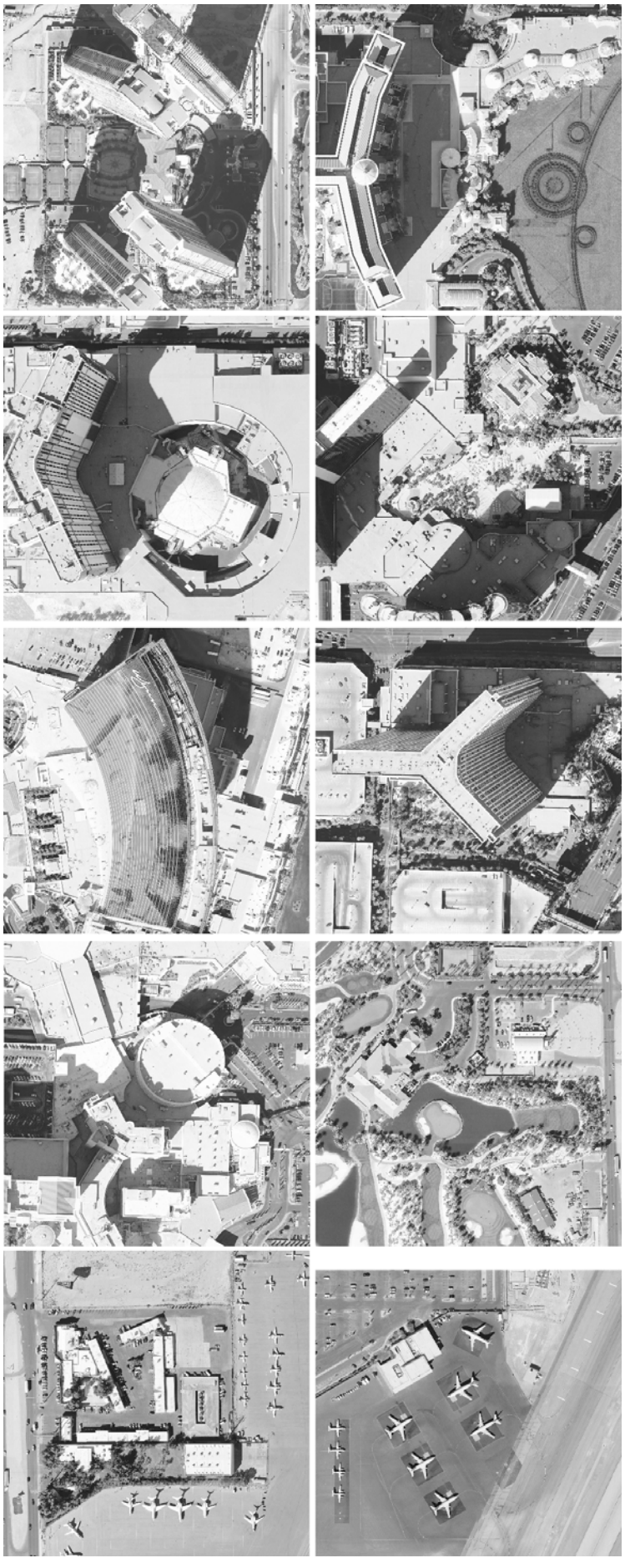

Appendix C

REAL IMAGES

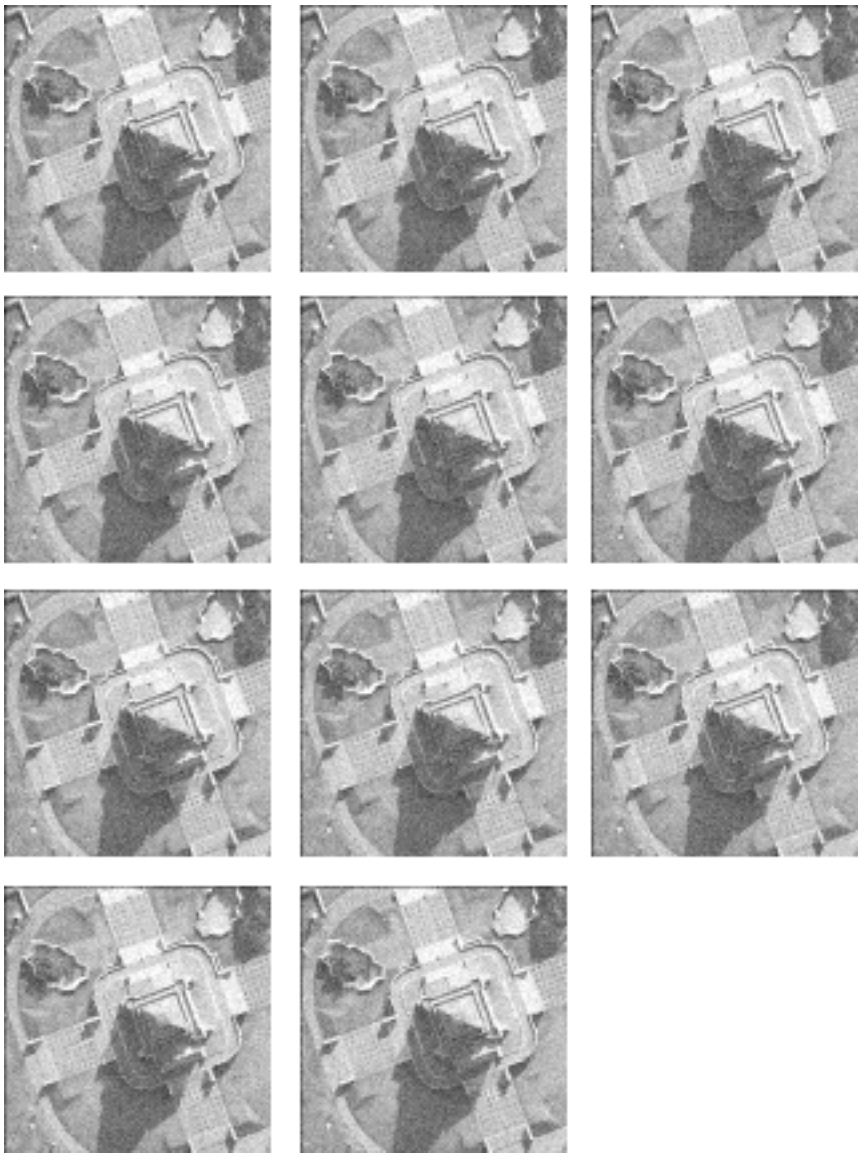

BIBLIOGRAPHY

[Bose93] N. K. Bose, H. C. Kim, and H. M. Valenzuela, “Recursive implementation of total least squares algorithm for image reconstruction from, noisy, under-sampled multi-frames,” in Proc. IEEE Int. Conf. Acoustics, speech, and Signal Processing, vol. 5 Apr. 1993, pp. 69–272.

[Borman98] S. Borman and R. L. Stevenson, “Super-resolution from image sequences—A review,” in Proc. Midwest Symp. Circuits and Systems, vol.5, Notre Dame, IN, Apr. 1998.

[Baboulaz09] L. Baboulaz, P.L. Dragotti, "Exact Feature Extraction Using Finite Rate of Innovation Principles With an Application to Image Super-Resolution,", IEEE Transactions on , Image Processing vol.18, no.2, pp.281-298, Feb. 2009.

[Costa09] G.H.Costa, J.C.M.Bermudez, "Registration Errors: Are They Always Bad for Super-Resolution,", IEEE Transactions on Signal Processing, vol.57, no.10, pp.3815-3826, Oct. 2009.

[Costa08] G.H. Costa and J.C.M. Bermudez, "Informed Choice of the LMS Parameters in Super-Resolution Video Reconstruction Applications," Signal Processing, IEEE Transactions on , vol.56, no.2, pp.555-564, Feb. 2008.

[Chiang00] M. C. Chiang, T. E. Boult, “Efficient super-resolution via image warping, Image and Vision Computing,” Volume 18, Issue 10, pp 761-771, July 2000.

[Dai09] S.Y. Dai, M. Han, W. Xu; Y. Wu, Y.H. Gong, A.K. Katsaggelos, "SoftCuts: A Soft Edge Smoothness Prior for Color Image Super-Resolution," Image Processing, IEEE Transactions on , vol.18, no.5, pp.969-981, May 2009.

[Elad97] M. Elad and A. Feuer, "Restoration of single super-resolution

image from several blurred, noisy and down-sampled measured images," IEEE Trans. Image Processing, vol. 6, no. 12, pp. 1646-1658, Dec.1997.

[Freeman02] W. T. Freeman, T. R. Jones, and E. Z. Pasztor, “Example-based superresolution,” IEEE Computer Graphic. Appl., vol. 22, no. 2, pp. 56–65, Mar. 2002.

[Farsiu04] S.Farsiu, M.D.Robinson, M.Elad, P.Milanfar, “Fast and robust multi-frame super resolution,” IEEE Trans. Image Process., vol. 13, no. 10, pp. 1327 - 1344, Oct. 2004.

[Farsiu06] S. Farsiu, M. Elad, and P. Milanfar, “Multiframe demosaicing and superresolution of color images,” IEEE Trans. Image Processing, vol. 15, no. 1, pp. 141–159, Jan. 2006.

[Fransens07] R. Fransens, C. Strecha, L.V. Gool, “ Optical flow based super-resolution: A probabilistic approach, Computer Vision and Image Understanding,” Volume 106, Issue 1, pp 106-115, Special issue on Generative Model Based Vision, April 2007.

[Fan06] C.Fan, J.J.Zhu, J.Y.Gong, C.L.Kuang, "POCS Super-Resolution Sequence Image Reconstruction Based on Improvement Approach of Keren Registration Method," Intelligent Systems Design and Applications, International Conference on, pp. 333-337, Sixth International Conference on Intelligent Systems Design and Applications (ISDA'06) Volume 2, 2006.

[Goldberg03] N. Goldberg, A. Feuer, G. C. Goodwin, Super-resolution reconstruction using spatio-temporal filtering, Journal of Visual Communication and Image Representation, Volume 14, Issue 4, pp. 508-525, December 2003.

[Huang84] T. S. Huang and R. Y. Tsai, “Multi-frame image restoration and registration,” Adv. Computer. Vis. Image Process., vol. 1, pp. 317–339, 1984.

[He07] Y. He, K.H. Yap, L. Chen, L.P. Chau, “A Nonlinear Least Square Technique for Simultaneous Image Registration and Super-Resolution,” IEEE Transaction on Image Processing, vol. 16, no. 11, pp. 2830 - 2841, Nov. 2007.

[Hardie98] R. C. Hardie, K. J. Barnard, J. G. Bognar, E. E. Armstrong, and E.A. Watson, “High-resolution image reconstruction from a sequence of rotated and translated frames and its application to an infrared imaging system,” Opt. Eng., vol. 37, no. 1, pp. 247–260, Jan. 1998.

[Hardie07] R.C. Hardie, “A Fast Image Supre-Resolution Algorithm Using an Adaptive Wiener Filter,” IEEE Transaction on Image Processing, Vol.16, No.12, pp.2953-2964, December 2007.

[He09] Y. He, K.H. Yap, L. Chen, L.P. Chau, A soft MAP framework for blind super-resolution image reconstruction, Image and Vision Computing, Volume 27, Issue 4, pp 364-373, March 2009.

[Irani91] M. Irani and S. Peleg, “Improving resolution by image registration,” CHIP: Graph. Models Image Process., vol. 53, no. 3, pp. 231–239, May 1991.

[Isakov06] V. Isakov, Inverse Problems for Partial Differential Equations, 2nd edition, New York: Springer Science + Business Media, Inc., c2006.

[Jiji06] C. V. Jiji and S. Chaudhuri, “Single-frame image super-resolution through contourlet learning,” EURASIP J. Appl. Signal Process., vol. 2006, no. 2, pp. 1–11, 2006.

[Jain 89] A.K.Jain, Fundamentals of Digital Image Processing, Englewood Cliffs, N.J. : Prentice Hall, 1989.

[Kim90] S. Kim, N. Bose, and H. Valenzuela, “Recursive reconstruction of high resolution image from noisy under-sampled multi-frames,” IEEE Trans. Acoustic, Speech, Signal Process., vol. 38, no. 6, pp.

1013–1027, Jun. 1990.

[Kim93] S. Kim and W. Su, “Recursive high-resolution reconstruction of blurred multi-frame images,” IEEE Trans. Image Process., vol. 2, no. 10, pp. 534–539, Oct. 1993.

[Keren88] D. Keren, S. Peleg, and R. Brada, “Image sequence enhancement using sub-pixel displacement,” in Proceedings IEEE Conference on Computer Vision and Pattern Recognition, pp. 742-746, June 1988.

[Kang03] M. G. Kang and S. Chaudhuri, “Super-resolution image reconstruction (guest editorial),” IEEE Signal Processing Magazine, special issue on super-resolution, vol. 20, no. 3, pp. 19–20, May 2003.

[Li10] X.L. Li, Y.T. Hu, X.B. Gao, D.C. Tao, B.J. Ning, A multi-frame image super-resolution method, Signal Processing, Volume 90, Issue 2, pp. 405-414, February 2010.

[Levy87] P.Levy, Calcul des Probabilities, Paris: Gauthier, 1987.

[Naray07] B.Narayanan, R.C.Hardie, K.E.Barner, M.Shao, “A Computationally Efficient Super-Resolution Algorithm for Video Processing Using Partition Filters,” IEEE Transaction on Circuit and System for Video Technology, Vol.17, No.5, pp.621-634, May 2007.

[Nguyen00] N. Nguyen and P. Milanfar, “A wavelet-based interpolation restoration method for superresolution,” Circuits, Syst., Signal Process., vol. 19, no. 4, pp. 321–338, Aug. 2000.

[Nguyen01] N. Nguyen, P. Milanfar, and G. H. Golub, “A computationally efficient superresolution image reconstruction algorithm.” IEEE Trans. Image Processing, vol. 10, no. 4, pp. 573–583, Apr. 2001.

[Ng06] M. Ng, T. Chan, M. G. Kang, and P. Milanfar, “Super-resolution imaging: analysis, algorithms, and applications (guest editorial),”

EURASIP Journal on Applied Signal Processing, special issue on super-resolution, vol. 2006, pp. Article ID 90 531, 2 pages, 2006.

[Nikias98] C.L.Nikias and M.Shao, Signal Processing with Alpha-Stable Distributions and Applications, New York City, NY : The Institute of Electrical and Electronics Engineers, Inc., 1998.

[Pham06] T. Q. Pham, L. J. van Vliet, and K. Schutte, “Robust fusion of irregularly sampled data using adaptive normalized convolution,” EURASIP Journal on Applied Signal Processing, 2006.

[Protter09A] M. Protter, M. Elad, H. Takeda, and P. Milanfar, “Generalizing the Non-Local-Means to Super-resolution Reconstruction”, *IEEE Trans. Image Processing*, vol. 18, no. 1, pp. 36-51 , Jan. 2009.

[Protter09B] M. Protter, M. Elad, "Super Resolution With Probabilistic Motion Estimation," Image Processing, IEEE Transactions on , vol.18, no.8, pp.1899-1904, Aug. 2009.

[Segall04] C. A. Segall, A. K. Katsaggelos, R. Molina, and J. Mateos, “Bayesian resolution enhancement of compressed video,” IEEE Trans. Image Process., vol. 6, no. 6, pp. 1–14, Jun. 2004.

[Shen07] H.F.Shen, L.P.Zhang, B.Huang and P.X.Li, “A MAP Approach for Joint Motion Estimation, Segmentation and Super Resolution,” IEEE Transaction on Image Processing, Vol.16 No.2, pp.479-490, February 2007.

[Sanchez08] A. Sanchez-Beato, G. Pajares, "Noniterative Interpolation-Based Super-Resolution Minimizing Aliasing in the Reconstructed Image,", IEEE Transactions on Image Processing, vol.17, no.10, pp.1817-1826, Oct. 2008.

[Tuinstra99] T. R. Tuinstra and R. C. Hardie, “High resolution image reconstruction from digital video by exploitation on non-global motion,” Opt. Eng., vol. 38, no. 5, May 1999.

[Takeda09] H. Takeda, P. Milanfar, M. Protter, and M. Elad, "Super-Resolution Without Explicit Subpixel Motion Estimation," Image Processing, IEEE Transactions on , vol.18, no.9, pp.1958-1975, Sept. 2009.

[Takeda07] H. Takeda, S. Farsiu and P. Milanfar, "Kernel Regression for Image Processing and Reconstruction," IEEE Transactions on Image Processing, vol.16, no.2, pp.349-366, Feb. 2007.

[Tappen03] M. F. Tappen and B. C. Russell and W. T. Freeman, “Exploiting the Sparse Derivative Prior for Super-Resolution and Image Demosaicing,” In IEEE Workshop on Statistical and Computational Theories of Vision, 2003.

[Tian10] J. Tian, K.K. Ma, Stochastic super-resolution image reconstruction, Journal of Visual Communication and Image Representation, In Press, Corrected Proof, Available online 7 January 2010.

[Tikh97] A.N.Tikhonov and V.Ya.Arsenin, “Solution of ill-posed problem,” Transl. from Russian, John Wiley & Sons, New York – Toronto, 1997.

[Vand07] P. Vandewalle, L. Sbaiz, J. Vandewalle, M. Vetterli, "Super-Resolution From Unregistered and Totally Aliased Signals Using Subspace Methods," Signal Processing, IEEE Transactions on , vol.55, no.7, pp.3687-3703, July 2007.

[Zomet01] A. Zomet and A. Rav-acha and S. Peleg,” Robust Super-Resolution,”, in In Proc. of the IEEE Workshop on Applications of Computer Vision, pp. 645—650, 2001.

[Zhang10] L.P. Zhang, H.Y. Zhang, H.F. Shen, P.X. Li, A super-resolution reconstruction algorithm for surveillance images, Signal Processing, Volume 90, Issue 3, pp. 848-859, March 2010.